Measurements of Malleable Visual Mechanisms Through High-resolution fMRI and Perceptual Learning

A Dissertation

SUBMITTED TO THE FACULTY OF

THE UNIVERSITY OF MINNESOTA

BY

Karen T. Navarro

IN PARTIAL FULFILLMENT OF THE REQUIREMENTS

FOR THE DEGREE OF

DOCTOR OF PHILOSOPHY

Advisor: Cheryl A. Olman, Ph.D. and Stephen A. Engel, Ph.D.

May 2023

Acknowledgments

First, I would like to express gratitude to my advisors, Dr. Stephen Engel and Dr. Cheryl Olman, who provided tremendous guidance and support and continuously advocated for me. I would also like to thank the other members of my dissertation committee, Dr. Gordon Legge, Dr. Kendrick Kay, and Dr. Vanessa Lee.

Thank you to everyone from both the Engel lab and the Olman lab. I especially want to thank Dr. Katherine Tregillus, who helped me tremendously. Without her incredible support, professionally and personally, I would not have completed this journey, and I look forward to a lifelong friendship with you. Special thanks to Dr. Jesse Breedlove, who went out of their way to help me, especially in this last stage of my degree. I want to thank Dr. Kimberly Weldon, who provided guidance through the early years of my degree. I would like to thank Joe Emerson and Yanjun Li, who collaborated with me on various projects and offered much-needed support.

I also want to thank the people outside of academia who helped me throughout the years, especially those in my CrossFit/weightlifting community. Thank you to my coach Danny who has pushed me to try movements and weights I did not know I could. Thank you to my friend and fellow athlete, Molly; our regular weekend morning hangs kept me sane for the last couple of years, and I look forward to many more.

I would especially like to thank my husband, Angel, who stood by my side for the last five years and supported me through some of the most challenging times. You are the only person who understood the struggles of my intersectional identity, and your

presence alone helped me immensely. I would also like to thank my parents for pushing me to pursue my passions even though you didn't understand them. You both moved to this country to provide me with a better life and worked tirelessly, at times to your physical limits, to provide me with the best education possible. I'll never be able to repay the sacrifices you two made for me, but I hope to provide you with the best-retired life. Last but not least, I would like to thank all of my pets: Addy, Lizzo, Michi, and Cisca, for being so sweet and goofy and always keeping me company during long workdays.

Preface

This dissertation contains three separate studies aimed at exploring the dynamic nature of visual properties. The first and second chapters explain two neuroimaging experiments using high-field resolution fMRI on human participants exploring how neuronal activity changes both across cortical space and across depth. The first study explored how stimulation by chromatic and achromatic stimuli changed responses across depth in the primary visual cortex (V1). The second study explores how orientation preference changes across the surface of V1 and how orientation selectivity changes across depth. The last chapter explores how eye dominance dynamics during binocular rivalry can change through perceptual learning. A follow-up neuroimaging study on these eye dominance dynamics was considered, but the behavioral results were not as reliable as needed to deem a neuroimaging study feasible.

Abstract

For many decades, low-level properties of the visual system, like orientation selectivity, were considered stable. However, advances in methodologies and theoretical frameworks have challenged this belief; we now know that external and internal factors can influence many low-level visual properties. I conducted three separate studies that looked at different visual properties using both behavioral and high-resolution neuroimaging methods, focusing on mechanisms in the primary visual cortex.

The first study explored laminar profiles of magnocellular and parvocellular pathways in human V1. This neuroimaging study used achromatic checkerboards with low spatial frequency and high temporal frequency to target the color-insensitive magnocellular pathway and chromatic checkerboards with higher spatial frequency and low temporal frequency to target the color-selective parvocellular pathway of V1. This work resulted in three main findings. First, responses driven by chromatic stimuli had a laminar profile biased towards superficial layers of V1, as compared to responses driven by achromatic stimuli. Second, we found a stronger preference for chromatic stimuli in parafoveal V1 compared with peripheral V1. Finally, we found alternating stimulus-selective bands stemming from the V1 border into V2 and V3.

The second study explored the orientation dependence of neural activity in human V1. This study measured responses to stimuli at different orientations to capture the orientation-tuning properties of V1 both across cortical space and through cortical depth. This work resulted in two main findings. First, we validated previous work that orientation preference can be predicted by retinotopic location (i.e., radial bias). Second, we captured

weak orientation selectivity across all depths in cortex and attribute this finding to the fact that fMRI responses reflect neural activity averaged over a finite volume of cortex.

The last study explored if temporal dynamics of sensory eye dominance could be altered using a perceptual learning technique. This study used orthogonal gratings during binocular rivalry to influence the temporal dynamics of sensory eye dominance through repeated training. Participants completed 12 days of a task meant to increase representation of one stimulus over the other. Temporal dynamics before and after training were compared. We found an increase in the total time participants spent seeing the grating from the trained eye and concluded that temporal dynamics can be changed through perceptual learning. However, this effect was relatively weak and varied in strength across participants.

Table of Contents

Acknowledgments ..... **i**

Preface ..... **iii**

Abstract ..... **iv**

Table of Contents ..... **vi**

List of Figures ..... **viii**

Chapter 1: Structural Measures of Magno- and Parvocellular Projections in Visual Cortex Using Ultra-High Field fMRI **1**

1. INTRODUCTION 1
2. METHODS 4
   - *2.1 Participants* *4*
   - *2.2 Apparatus* *4*
   - *2.3 Experimental Design* *5*
   - *2.4 Data Collection* *8*
   - *2.5 Data pre-processing* *10*
   - *2.6 Data analysis* *12*
3. RESULTS 18
4. DISCUSSION 22

Chapter 2: Orientation Selectivity in Visual Cortex Using Ultra-High Field fMRI **28**

1. INTRODUCTION 28
2. METHODS 31
   - *2.1 Participants* *31*
   - *2.2 Apparatus* *31*
   - *2.3 Experimental Design* *31*
   - *2.4 Data collection* *36*
   - *2.5 Data pre-processing* *37*
   - *2.6 Data Analysis* *38*
3. RESULTS 43
4. DISCUSSION 46

Chapter 3. Perceptual Learning Can Manipulate Binocular Rivalry Dynamics **52**

1. INTRODUCTION 52
2. METHODS 55
   - *2.1 Participants* *55*
   - *2.2 Apparatus and stimuli* *55*
   - *2.3 Experiment Timeline* *57*
   - *2.4 Eye dominance session* *58*
   - *2.5 Pre/post-training sessions* *58*
   - *2.6 Training sessions* *59*
3. RESULTS 59
   - *3.1 Pre/post-training rivalry task* *59*
   - *3.2 Aspect ratio task* *64*

4. DISCUSSION.....66
References 71

List of Figures

Figure 1. Examples of each stimulus display. 6

Figure 2 Retinotopic mapping of V1 and manually drawn ROIs.....13

Figure 3. Assignment of gray matter and voxel depth locations.....16

Figure 4. Responses to chromatic and achromatic stimuli in V1.....18

Figure 5. Laminar profiles of differential responses to chromatic vs achromatic stimuli in V1 as a function of eccentricity.....20

Figure 6. Repeatability of extrastriate bands across days for two participants.. 21

Figure 7. Stimulus spatial configuration. 32

Figure 8. Single-trial timeline. 33

Figure 9. Visual conditions and block structure for task and localizer scans. 35

Figure 10. Target ROI delineation.. 41

Figure 11. Orientation selectivity across depth in V1.. 44

Figure 12. Orientation tuning distributions within the ROIs in V1 and visual space.. 45

Figure 13. Evaluation of OSI distribution. 49

Figure 14. Visual stimuli and time course for each task. 57

Figure 15. Percept durations distributions for each participant and rivalry session for trained and untrained eyes combined. 60

Figure 16. Mean percept durations for each rivalry session and each state. 62

Figure 17. Mean total durations for each rivalry session and each state across blocks.63

Figure 18. Mean durations for the untrained configuration.....64

Figure 19. Mean percept durations in the aspect ratio task across training sessions. ...65

Figure 20. Mean total block durations in the aspect ratio task across training sessions. 66

Chapter 1: Structural Measures of Magno- and Parvocellular Projections in Visual Cortex Using Ultra-High Field fMRI

1. Introduction

The visual system uses parallel processing to transmit visual input from the retina to the visual cortex (Desimone et al., 1985; Maunsell, 1987; Mishkin et al., 1983; Shipp & Zeki, 1985; Yabuta et al., 2001). Past research has demonstrated that at least three major pathways work together to transmit this information: the parvocellular (P), magnocellular (M) and koniocellular (K) pathways(Callaway, 2005; M. Livingstone & Hubel, 1988; Norton & Casagrande, 1982; Schiller & Logothetis, 1990; Silveira et al., 2004). All three pathways begin with specific subtypes of ganglion cells that project from the retina to the lateral geniculate nucleus (LGN) and continue from the LGN to the primary visual cortex (V1) (Dacey & Lee, 1994; Kandel et al., 2000). The neuronal sensitivity profiles in each pathway overlap, so no visual experience will drive a single pathway in isolation. In the present experiment, color and luminance contrast and temporal frequency were manipulated to create stimuli that would minimize responses in the K pathway and differentiate between responses in putative P and M pathways in early visual areas.

The primary goal of the present work was to use depth-dependent fMRI(Huber et al., 2017; Kok et al., 2016; Olman et al., 2012, 2018; Uğurbil et al., 2003) to establish how sensitivity to color in human V1 depends on cortical depth. Stimuli with chromatic contrast and relatively low temporal frequencies will preferentially stimulate the P pathway

(Derrington & Lennie, 1984; Hubel & Livingstone, 1990; Kaplan & Shapley, 1982), which projects from the dorsal layers of LGN into layer 4Cβ of V1 and then to the cytochrome oxidase-rich blobs in the deep and superficial layers 2/3 of V1. The M pathway, which is relatively color insensitive and tuned to higher temporal frequencies (Calkins et al., 1994; Chatterjee & Callaway, 2003; Martin et al., 1997), projects from the ventral layers of LGN into layer 4Cα of V1, then to layer 4B, and then to the extrastriate cortex (Blasdel & Lund, 1983; Callaway & Wiser, 1996; Nassi & Callaway, 2009; Yabuta & Callaway, 1998). Therefore, because red/green stimuli contrast-reversing at 0.5 Hz and the black/white stimuli alternating at 12 Hz will produce responses biased toward the P and M pathways, respectively, different depth-dependent fMRI responses are expected for the stimuli used in this study.

An additional goal of the present study was to measure how the relative contributions of responses driven by chromatic and achromatic stimuli change as a function of eccentricity in V1. Decreasing sensitivity to red-green color contrast with increasing eccentricity has been measured behaviorally(Anderson et al., 1991; Mullen, 1991; Mullen & Kingdom, 2002; Newton & Eskew, 2003), and it has been hypothesized that this eccentricity preference is due to decreased P inputs to peripheral V1 (Mullen & Kingdom, 1996; Vanni et al., 2006). Similarly, the transient channels of the M pathway are more sensitive to fast flickers, and behavioral studies show that human observers are more sensitive to fast flicker in peripheral vision(McKee & Taylor, 1984; Snowden & Hess, 1992). It has also been shown using 3T fMRI that fast flicker produces a consistent BOLD signal across eccentricity of V1, while slowly alternating stimuli elicit a stronger signal in the fovea and weaker signal in the periphery (Horiguchi et al., 2009). Thus, slowly

alternating, chromatic stimuli should elicit the strongest fMRI responses in foveal regions of V1, with the relative response to rapidly alternating, achromatic stimuli increasing in peripheral V1.

The visual features that differentiate putative M and P pathways in V1 have also been shown to cause a repetitive alternating pattern of stripes along V2. Interleaved thin (color-selective), thick (stereo-selective), and pale (form-selective) stripes of oxidase staining have been found with a repeating pattern of pale-thick-pale-thin in V2 of NHP (An et al., 2012; Chen et al., 2008; Hubel & Livingstone, 1985; M. Livingstone & Hubel, 1988; Lu & Roe, 2007; Salzmann et al., 2012; Vanduffel et al., 2002; Xiao & Felleman, 2004). Similar stripe-based subdivisions have been found in human V2 for selectivity of several features like temporally selective stripes (Dumoulin et al., 2017), disparity-selective stripes (Nasr & Tootell, 2018; Tootell & Nasr, 2017), and color-selective stripes (Nasr et al., 2016; Tootell & Nasr, 2017). These stripes terminate at the V1/V2 border. NHP studies have found at least three types of structures that project from V1 into V2: interblobs in the superficial layers of V1 project equally to thick and pale stripes; layer 4B of V1 has a significant projection to thick stripes; blobs in the superficial layers of V1 project to thin stripes(Burkhalter & Bernardo, 1989; M. Livingstone & Hubel, 1988; Nassi & Callaway, 2007; Roe & Ts'o, 1995; Sincich et al., 2010; Sincich & Horton, 2002; Tootell et al., 1983). Thus, in NHPs the M-pathway dominates thick stripes and the P pathway contributes more strongly to thin stripes.

NHP histology (Burkhalter & Bernardo, 1989; Nassi & Callaway, 2007; Sincich et al., 2010; Sincich & Horton, 2002; Tootell et al., 1983) and imaging studies (Li et al., 2019)

have measured the spacing of these stripes to be about 4 mm from the center of a thick stripe to the center of a thick stripe. Human histology (Adams et al., 2007; Burkhalter & Bernardo, 1989; Hockfield et al., 1990; Tootell & Taylor, 1995) and neuroimaging studies (Dumoulin et al., 2017; Nasr and Tootell, 2016; Tootell and Nasr, 2017) have found these stripes to have spacing ranging from 4 mm to 8 mm from one thick stripe to its adjacent thick stripe. In addition to imaging the laminar profiles of responses to chromatic and achromatic stimuli as a function of eccentricity in V1, this study was able to verify the appearance of these stripes at the V1/V2 border.

2. Methods

2.1 Participants

Seven neurotypical adults (five females) aged 23 to 50 years old participated in the experiment. All experimental procedures were approved by the University of Minnesota's Institutional Review Board. Written informed consent was obtained from all participants before the experiments. Participants were compensated at a rate of $20 per hour. Each participant was scanned two or three times for validation.

2.2 Apparatus

The stimuli were presented using a VPixx PROPixx projector. Participants wore polarized glasses that allowed for dichoptic presentation of the stimuli. The dichoptic presentation of the stimuli facilitated a separate, simultaneous experiment studying eye selectivity through the cortical depth. During any given block stimuli were presented to one eye (the background gray screen, with only a fixation mark, was presented to the

other) at an effective frame rate of 60 Hz in the eye that was receiving stimulus. The stimuli were projected onto a polarization-preserving screen placed in the magnet bore behind the participant's head, which was viewed via a mirror situated above the participant's eyes. The screen was 85 cm from the participant's eyes, and the rectangle in which stimuli were presented was 46 cm × 26 cm.

2.3 Experimental Design

2.3.1 Visual Stimuli Two types of visual stimuli were presented with the intent of differentiating responses in putative P and M pathways (Denison et al., 2014; Olman et al., 2012)(Denison et al., 2014; Olman et al., 2012). Achromatic checkerboards with high contrast (70.3%) and lower spatial frequency (~1 cycle per degree (cpd) in the parafovea) flickering at higher temporal frequency (12 Hz) targeted the M pathway (Figure 1A). The highest spatial frequencies were removed from the achromatic stimulus by blurring with a Gaussian kernel with a sigma of 0.2°. Chromatic (green and red) checkerboards with low luminance contrast (4.6%) and higher spatial frequency (check size was doubled, and edges were not removed by blurring) flickering at low temporal frequency (0.5 Hz) targeted the P pathway (Figure 1B). The color values chosen for the chromatic stimuli were nominally isoluminant in CIELAB space and presented with a color calibrated system; actual luminance values were measured with a spectrophotometer through the polarized lenses worn by participants.

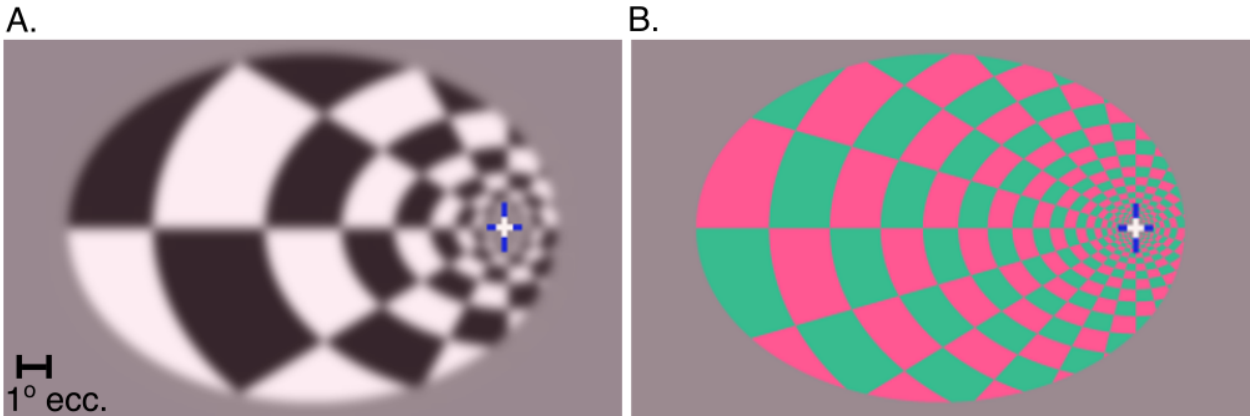

Figure 1. Examples of each stimulus display. A) Visual stimulus that targeted the M pathway (achromatic, lower spatial frequency, and higher temporal frequency (12 Hz). B) Visual stimuli that targeted the P pathway (lower luminance contrast, higher chromatic contrast, increased spatial frequency, alternating at 0.5 Hz).

Typically, stimuli targeted at the M system have low contrast in order to provide weak drive to the P pathway. However, our previous work (Olman et al., 2012) found that the overall fMRI response amplitude to chromatic stimuli was much larger than the response to low-contrast achromatic stimuli (possibly because elaboration of the capillary bed is known to follow CO staining (Keller et al., 2011; Murphy et al., 2001), so we used higher contrast for the achromatic stimuli to elicit fMRI responses of similar magnitude in both conditions.

The checkerboard patterns were placed in an oval-shaped aperture on a gray background. A fixation cross was situated to one side of the stimulus; this design allowed stimulation out to 20° of visual angle on one side of the visual field (at the expense of the other). During the scan, participants were asked to maintain fixation on the cross and report via button press whenever the colors of the cross periodically reversed. The size of the checks was scaled so they were larger at higher eccentricities, doubling in size as eccentricity doubled from the fixation point into the periphery to roughly accommodate

increasing receptive field sizes (and decreasing spatial frequency preferences) in both the putative M and P pathways.

It is known that the perceptual isoluminance point varies across the visual field (Bilodeau and Faubert, 1997; Livingstone and Hubel, 1987b; Mullen, 1985). The stimuli were not varied across the visual field to try to accommodate this variance because individual differences in cortical magnification, isoluminance, and subtle variations in the quality of the projected image tend to confound attempts to equate effective luminance contrast (unwanted drive to putative M pathways by the chromatic stimuli) as a function of eccentricity. Instead of measuring isoluminance values at several eccentricities for each observer and customizing the stimuli accordingly (Nasr et al., 2016), we chose to present stimuli that had low but non-zero luminance contrast throughout the visual field.

To confirm that the effective luminance contrast of the red/green colors used in the chromatic stimuli was between 5 and 10% across the range of eccentricities measured, we asked 3 of the observers to perform a contrast detection task in which either red and green patches or black and white patches were alternated in parafoveal, middle, or peripheral regions of the visual stimulus field at 30 Hz. The flicker detection threshold for the black/white colors was 7% of the level used for the main experiment (SD = 2%) in parafoveal regions, 4% (SD = 0.5%) at 5–15° eccentricity, and 5% (SD = 0.7%) beyond 15° eccentricity. These values equate to contrast detection thresholds of 3–5% luminance contrast.

For the red/green colors, the detection thresholds were 54% (SD = 3%), 48% (SD = 7%) and 50% (SD = 7%) of the levels used in the main experiment, in the parafoveal,

middle, and peripheral regions, respectively. From this we conclude that the effective luminance contrast of the chromatic stimuli was twice the threshold, on average, and roughly 10 times lower than the measured 70% luminance contrast of the achromatic stimuli. In addition, we did not measure significant variation in the effective contrast across 1–20° eccentricity, consistent with the data in Bilodeau & Faubert, 1997.

2.4 Data Collection

Functional MRI data were collected at the University of Minnesota's Center for Magnetic Resonance Research on a Siemens 7T scanner equipped with a custom-made head coil (32-channel transmit, 4-channel receive) (Adriany et al., 2012) that was used for T2∗-weighted gradient echo (GE) echo-planar imaging (EPI). Images were acquired with a coronal orientation in 36 slices positioned near the occipital lobe. Image resolution was 0.8 mm isotropic (field of view (FOV): 129.6 mm × 160 mm; matrix size: 162 × 200); the data were acquired with an in-plane parallel imaging acceleration factor (R) of 3 and a right-left phase-encode direction (6/8 Partial Fourier, echo-spacing: 1.01 ms). The repetition time (TR) was 2 s and the echo-time (TE) was 23.4 ms.

Each functional scan consisted of four conditions: achromatic stimuli presented to the left eye (AL), achromatic stimuli presented to the right eye (AR), chromatic stimuli presented to the left eye (CL), and chromatic stimuli presented to the right eye (CR). Within one scan all conditions including rest blocks were presented four times in pseudorandom order. Each condition was presented in 16 s blocks so that the scan lasted 320 s. A total of 10 functional scans were conducted during a session.

During each scanning session, we also acquired (1) a short phase encode reversed (left-right) EPI sequence to assist in distortion compensation during data preprocessing, and (2) a T1-weighted GE EPI (T1wEPI) sequence scan (van der Zwaag et al., 2018). Since both the T1wEPI data and the functional data were collected during the same session with the same resolution, sampling, and echo spacing, they were subject to the same distortion. The T1wEPI sequence was used to define the gray matter (GM) in the functional data.

We acquired a whole-brain T1-weighted MP-RAGE (Mugler III & Brookeman, 1990) during the session as an additional anatomical scan (1.0-mm isotropic, TR = 3100, TE = 3.27, flip angle = 6°, FOV = 156 × 192). A structural scan was acquired separately for all participants on a Siemens 3T scanner (0.8-mm isotropic T1-weighted MP-RAGE). Each participant completed two additional population receptive field (pRF) mapping scans (Dumoulin & Wandell, 2008) for the purpose of retinotopic mapping in a separate scanning session. During the task, participants were asked to maintain fixation on a central point while a bar moved across the visual field at one of eight orientations (Left Right, Top Left – Bottom Right, Top – Bottom, Top Right -Bottom Left, Right-Left, Bottom Right –TopLeft, Bottom –Top,Bottom Left -Top Right) in forward and reverse directions (e.g., Top – Bottom vs. Bottom –Top),for a total of 16 directions. The moving bar was populated with dynamic and highly salient visual stimuli from one of three categories (faces, objects, or noise) flickering at either 2 or 12 Hz. The bar spanned the visual field (out to 8° eccentricity) and subtended 2° of visual angle in width. Each bar took 16 s to complete the movement across the visual field, and each bar sweep direction occurred

once in a scan. There were 4 s of rest between each bar sweep and 4 s of rest at the beginning and end of each scan such that each scan took 324 s.

The two pRF scans used a GE EPI sequence that captured the whole brain. The pRF images were acquired at 1.4 mm isotropic resolution with a coronal slice orientation in 56 slices (FOV: 160 mm × 129 mm; matrix size: 114 × 92). The data were acquired with an in-plane parallel imaging acceleration factor (R) of 3 and a right-left phase-encode direction (6/8 Partial Fourier, echo-spacing: 1.01 ms). The repetition time (TR) was 2 s and the echo-time (TE) 22.6 ms.

2.5 Data pre-processing

2.5.1 Pre-processing 3T data We segmented the 3T reference anatomy to define the GM/white matter (WM) boundary and the pial surface using FreeSurfer's `recon-all` command (https://surfer.nmr.mgh.harvard.edu/, v6.0.0).

2.5.2 Pre-processing functional data Functional data were processed using tools provided by AFNI (https://afni.nimh.nih.gov/afni, v18.2.04). Motion compensation was performed using AFNI's `3dvolreg` to register all scans to the mean image of the functional scan acquired before the distortion-compensation (reversed phase-encode) scan. The 3T anatomy and the 7T T1wEPI were aligned to the motion compensated functional data. This was done by first registering the 3T anatomy to the 7T anatomy (coarsely aligned to the functional data) using `3dAllineate`. This step generated a transformation matrix that was used to generate an initial registration of the 3T anatomical reference volume to the functional data, which was refined by a second call to `3dAllineate` (lpc cost function). We processed the data from the 7T T1wEPI by

fitting each voxel's intensity as a function of the slice-specific inversion time for each volume acquisition. The processed T1wEPI (a T1 map) was then aligned to the functional data.

At this point, the cerebellum was stripped out of the T1wEPI using the 3T anatomy as reference. We then segmented the T1wEPI volumes using `3dSeg` (initializing the segmentation with GM/WM/CSF masks derived from the FreeSurfer segmentation on the 3T anatomy) so that each voxel was classified as GM, WM, or cerebral spinal fluid (CSF). As the T1wEPI was subject to the same distortion as the functional data but has better GM/WM contrast, this segmentation was used to define the GM in the functional data space.

Distortion compensation was performed for the functional data using the `3dQwarp` command, using the T1wEPI GM to generate a nonlinear WARP volume to optimize the GM registration between the functional and anatomical data. The WARP volume was then combined with the motion correction parameters to produce motion- and distortion-corrected fMRI data with a single resampling step.

A GM overlap mask was created by selecting the surface nodes where the T1wEPI GM marker was present throughout at least 75% of the GM in the reference anatomy and projecting those nodes through the cortical depth (Weldon et al., 2019). This mask ensured that depth-dependent analyses were performed only in regions with good registration between functional and anatomical data, since depth information was derived from a separate anatomical scan.

A binary veins mask was created by taking the average signal-to-noise ratio (SNR) map processed functional data and marking any voxel with SNR below 11. Visual inspection verified that only voxels near large veins and on movement-prone edges of the brain were marked after this step (Olman et al., 2007). This mask was then projected through the cortical depth to mark voxels that should not be included in laminar analyses because they were underneath or adjacent to large veins.

2.5.3 Pre-processing pRF data The retinotopic mapping scans were pre-processed using a pipeline similar to the sub-millimeter data. Distortion compensation was executed using AFNI's `3dQwarp` function which nonlinearly warped the functional pRF scans with a phase-encode reversed reference scan. Motion compensation was performed using AFNI's `3dvolreg` function. The anatomical data were aligned to the corrected functional data with AFNI's `3dAllineate` function. The amplitude values of the functional data were converted to percent signal change and demeaned.

2.6 Data analysis

2.6.1. pRF analysis and ROI delineation pRF analyses were conducted using custom tools designed and implemented in AFNI (see, Silson et al., 2015). We used the resulting retinotopic maps to verify that the V1 boundaries defined by a publicly available probabilistic atlas were accurate (Wang et al., 2015). Using the V1 boundary and eccentricity maps generated from the pRF data as a guide, we manually segmented V1 into parafoveal, middle, or peripheral regions of interest (ROIs) (Figure 2A). The average size of the parafoveal ROIs was 1660 voxels (SD=207 n = 10); the average size of the mid-eccentricity ROIs was 1660 voxels (SD=282, n = 10); the average

size of the peripheral ROIs was 1780 voxels (SD=289, n = 10). After restricting the ROIs to voxels associated with surface nodes where alignment was good, large veins were absent, activation was present throughout the cortical depth, and alignment was good, an average of 691 (SD=191, n = 10), 889 (SD=202, n = 10), and 732 (SD-216, n = 10) voxels were used for parafoveal, middle, and peripheral ROIs, respectively.

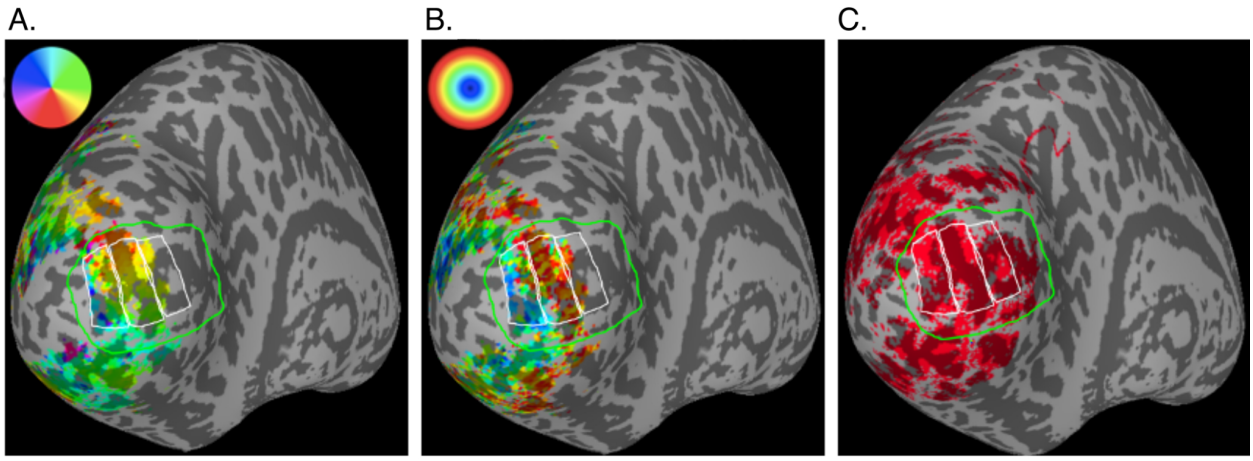

Figure 2 Retinotopic mapping of V1 and manually drawn ROIs.In each panel, the green line borders the probabilistic topography of V1 (Wang et al., 2015) and the white lines indicate the parafoveal (~2–4° eccentricity), middle (~4–8°), and peripheral (~8–20°) ROIs. A) The color overlay indicates polar angle estimated from pRF mapping scans. This was used to verify the location of the V1 border. B) The color overlay indicates estimated eccentricity from the pRF mapping scans, in which stimuli did not go beyond 8° eccentricity because the fixation point was in the center of the screen and the stimulus was circular. C) Red indicates a binary mask of activation from the main experiment ($p < 0.001$ single-voxel F-statistic, $p < 0.001$ after cluster-wise correction for multiple comparisons). In the functional scans, participants fixated on one side of the screen, so stimuli extended to 20° eccentricity. Therefore, the peripheral ROI was drawn past the extent of the retinotopy data to include the full extent of the data from the main experiment.

2.6.2. General linear model analysis The data were analyzed with a standard general linear model (GLM) using AFNI's `3dDeconvolve` to estimate the amplitude of response (percent signal change) during each of the four conditions (AL, AR, CL, CR) via linear regression against a model that was a hemodynamic response

function [hrf = tˆ4∗exp(-t)/(4ˆ2∗exp(−4)] convolved with a boxcar function representing the 16-second blocks of stimulus presentation. Voxels not significantly modulated by visual stimulus presentation ($p < 0.001$, uncorrected; cluster-wise correction, $p < 0.001$) were excluded from further analyses. In addition, surface nodes for which significant modulation was not present in at least 75% of the GM depth under the node were excluded from depth-dependent analyses.

Although stimuli were presented separately to participants' left and right eyes, to enable a separate study of ocular dominance, we collapsed across eye-of-presentation for the present analysis to estimate responses to chromatic and achromatic stimuli [C = (CL + CR)/2; A = (AL + AR)/2]. Selectivity for chromatic stimuli in each voxel was defined as the normalized difference in responses to chromatic and achromatic stimuli: selectivity = (C - A)/(C + A)/2.

2.6.3 Depth-dependent analysis For the depth dependent analyses, only data from the contralateral hemisphere (i.e., corresponding to the hemifield with more extensive stimulation) were analyzed. All voxels in an ROI were combined to provide a single estimate at each depth for each participant. We excluded any dataset with total motion greater than 2 mm (root-mean-square across the 3 Cartesian directions) and any dataset with fewer than 2500 significantly modulated voxels across the 3 ROIs. Four datasets were excluded due to excessive motion, and 2 were excluded due to an insufficient number of significantly modulated voxels; thus, we included 10 out of the original 16 datasets in our subsequent analyses.

We segmented the GM derived from the 3T anatomy into 10 depths using an equivolume solution (Waehnert et al., 2014) implemented in FreeSurfer (https://github.com/kwagstyl/surface_tools). These depths were projected into the space of the functional data (Figure 3). Each functional voxel was assigned a depth depending on its registration to the anatomical GM. We used the fine segmentations with smoothed data only for visualizing the overall pattern of functional responses across GM and not for statistical analyses. At 0.8 mm isotropic, our resolution was too coarse to define depth bins that actually correspond to the 6 histological layers of the GM. Therefore, only the functional responses at the most superficial and deepest layers were used for depth-dependent statistical analyses.

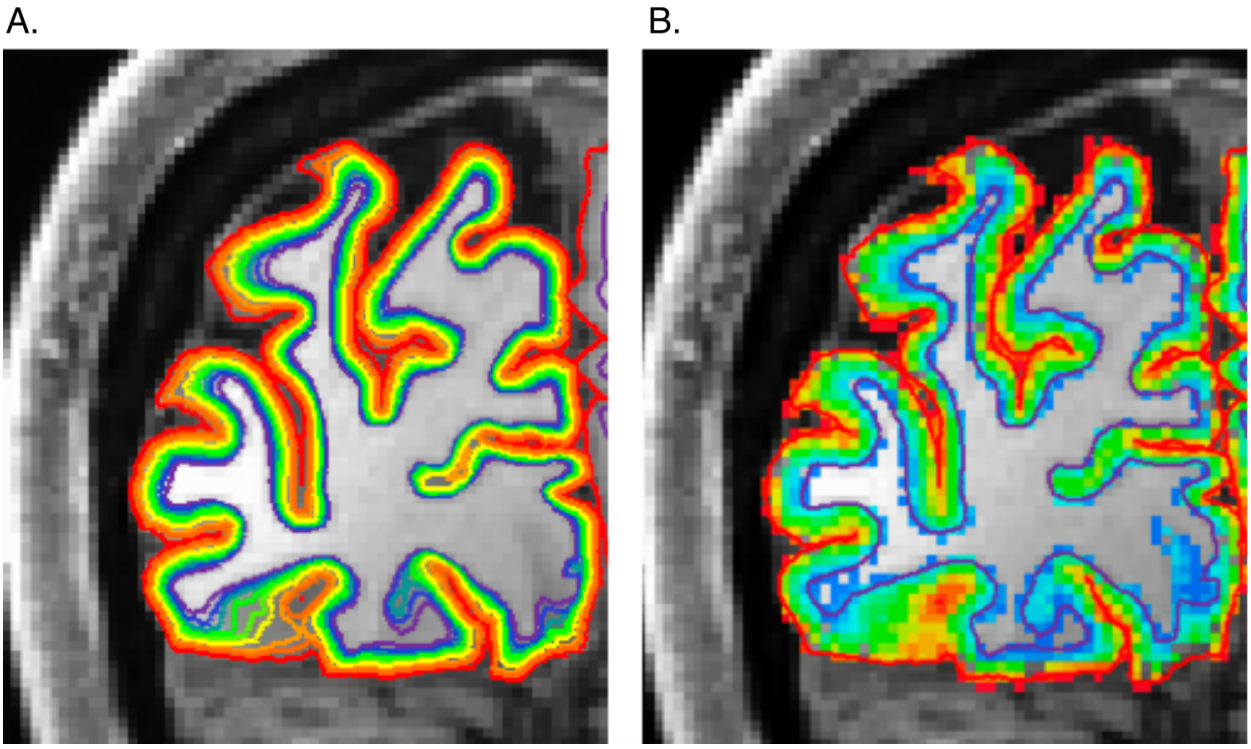

Figure 3. Assignment of gray matter and voxel depth locations. A) Each colored line represents a depth location inside the gray matter of one hemisphere relative to the white matter. B) All GM voxels are color-coded for their depth location where red is closest to the pial and purple is closest to the white matter.There were five necessary components to create accurate depth-dependent profiles: hand-drawn ROIs (Figure 2A), the GM overlap mask that ensured accurate functional/anatomical data registration for GM depth assignment, the significance mask, the vein-exclusion mask, and the GM depth assignment for each voxel. The GM overlap mask, significance mask, and vein-exclusion mask were combined to select the voxels analyzed within each ROI.

Statistical analysis was conducted with R Studio. Our dependent variable was selectivity for chromatic stimuli (i.e., percent signal change for the contrast (C - A)/(C + A)/2. A two-way analysis of variance was conducted to test for main effects of ROI (parafovea, middle, periphery) and Depth (Superficial or Deep layer) and for any interaction.

2.6.4. Stimulus-selective band analysis We observed alternating bands of activation selective to chromatic/achromatic stimuli along the dorsal and ventral border of V1 (Figure 4). We characterized the size and pattern of these bands on each hemisphere for each scanning session by manually selecting the start and end of each band when visualizing the data using AFNI's surface mapper (https://afni.nimh.nih.gov/Suma, v18.2.04). We manually marked the proximal and distal ends of each band (with proximal being defined as the end closest to the V1/V2 border) and quantified the distance between the center of bands for 6 datasets for which the bands were visible past the dorsal boundary of V1 border and for 8 quarterfield representations past the ventral boundary of V1.

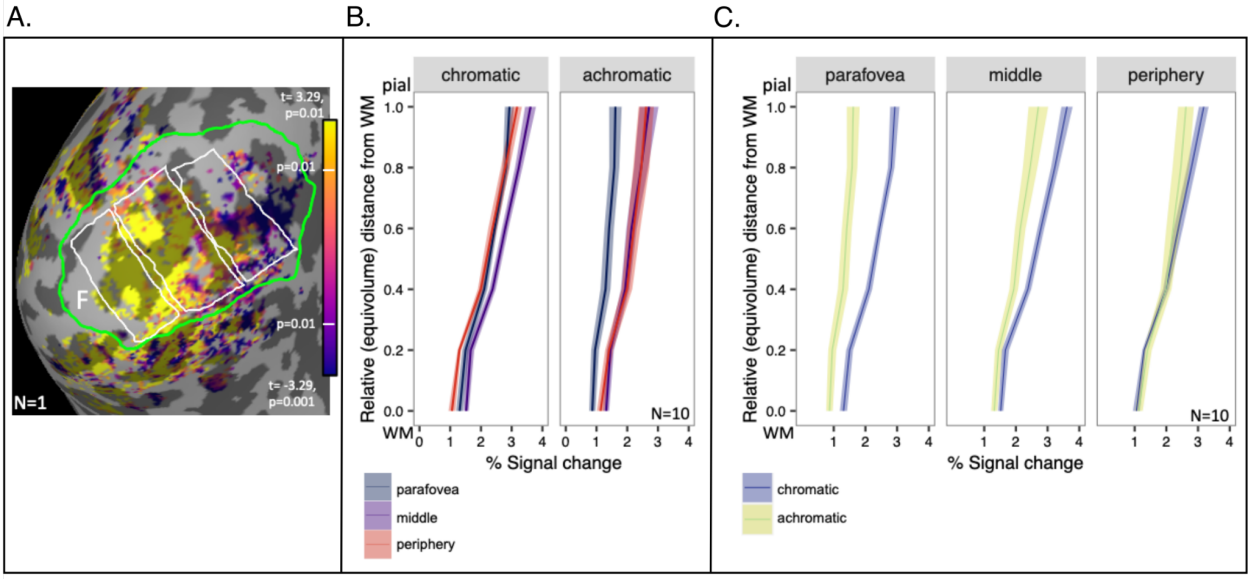

Figure 4. Responses to chromatic and achromatic stimuli in V1. A) T-statistics for chromatic selectivity are displayed for one participant (S1) on an inflated representation of the medial aspect of occipital cortex of the left hemisphere. Surface nodes with significant visual responses to all stimuli ($p < 0.001$, after cluster-wise correction) are displayed in color on an inflated representation of occipital lobe, where dark gray indicates sulci and light gray indicates gyri. Foveal retinotopic cortex is labeled with the letter "F". Parafoveal, middle, and peripheral ROIs are indicated by white borders (parafoveal is the leftmost ROI adjacent to the fovea). The V1 boundary is indicated by a green border. B) Estimates of the magnitude of responses to chromatic and achromatic stimuli in each of the three ROIs. Data represent responses from the 10 datasets (hemispheres) meeting all inclusion criteria; shading indicates standard error of the mean. C) The same data as in (B) are plotted again, grouped so comparisons between chromatic and achromatic responses can be made within each of the 3 ROIs.

3. Results

Both visual stimuli elicited robust responses throughout V1 (Figure 4A), with the response to the achromatic stimulus increasing with increasing eccentricity (parafovea < periphery, $t(19)= -4.433$, $p<0.001$). On the other hand, responses to the chromatic stimulus showed no significant difference between the parafovea and periphery ($t(19)= -0.002$, $p = 0.999$) (Figure 4B). The result of this was that the chromatic stimulus

dominated parafoveal regions, and response differences were smallest in the peripheral ROI (Figure 4C).

We characterized the difference between responses to chromatic stimuli and achromatic stimuli by computing a selectivity index, which was the difference between the two responses normalized by the average of the two responses. Even after normalization, stronger responses to chromatic stimuli were most pronounced in superficial layers (Figure 5A). Because the fMRI voxels are relatively large compared to the GM thickness, statistical tests were only performed using the most superficial and deepest depth bins (Figure 5B). There was a significant main effect of ROI ($F(2, 18) = 10.413$, $p < 0.001$, $\eta p2 = 0.761$) and a main effect of Depth ($F(1, 9) = 29.159$, $p < 0.001$, $\eta p2 = 0.886$) on chromatic selectivity with no interaction ($F(2, 18) = 0.087$, $p = 0.917$, $\eta p2 = 0.225$). This result demonstrates that chromatic selectivity varies across eccentricity in V1 and is significantly different in superficial and deep layers of the GM. A Bonferroni correction for multiple comparisons ($\alpha = 0.05/3 = 0.005$) was applied to post hoc analyses following up the main effect of ROI (collapsed across Depth). Chromatic selectivity was greater in the parafoveal ROI than the peripheral ROI ($p < 0.001$), indicating chromatic selectivity decreased with eccentricity in V1. When analyzing chromatic selectivity across Depth (collapsed across ROI) we found greater chromatic selectivity in superficial layers than in deep layers ($p < 0.001$).

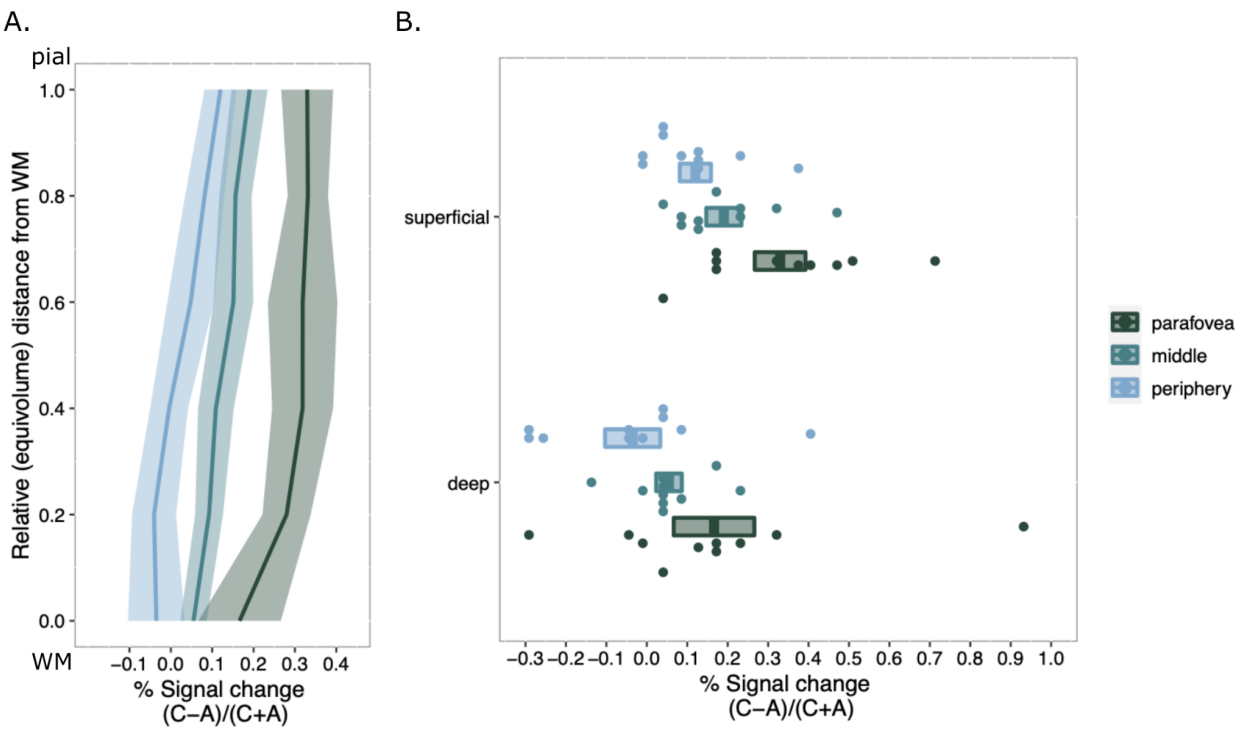

Figure 5. Laminar profiles of differential responses to chromatic vs achromatic stimuli in V1 as a function of eccentricity. (A) Differences were normalized by the average of both responses to eliminate dependence on overall BOLD response amplitude as a function of depth or eccentricity. Profiles were computed separately for parafoveal, middle, and peripheral ROIs. The shaded area around each profile is the standard error (n = 10). (B) Individual subject signal change is displayed as single points for the most superficial layer and the deepest layer. Significant differences are discussed in main text.

We observed periodic, stimulus-selective bands adjacent to and orthogonal to both the dorsal and ventral boundaries of primary visual cortex (Figure 6), consistent with previous reports (Dumoulin et al., 2017; Nasr and Tootell, 2016; Tootell and Nasr, 2017). The average spacing of bands on the dorsal side of V1 was 7.5 mm (SEM=0.32, n = 6); the average spacing of bands on the ventral side of V1 was 7.8 mm (SEM=0.54, n = 8). These values are within the range of spacing (4–8 mm) reported from measurements in post-mortem human brains (Adams et al., 2007; Burkhalter and Bernardo, 1989; Hockfield et al., 1990; Tootell and Taylor, 1995). The bands were observed in the same locations in different scanning sessions for a given participant (Figure 6), indicating that

they are likely a true measure of the underlying neural architecture and not an imaging artifact. We also computed depth-dependent analyses of chromatic selectivity within two band types (i.e., by treating bands selective for chromatic stimuli and bands selective for achromatic stimuli as different ROIs). We found no significant difference in laminar profiles of stimuli-selectivity between band types.

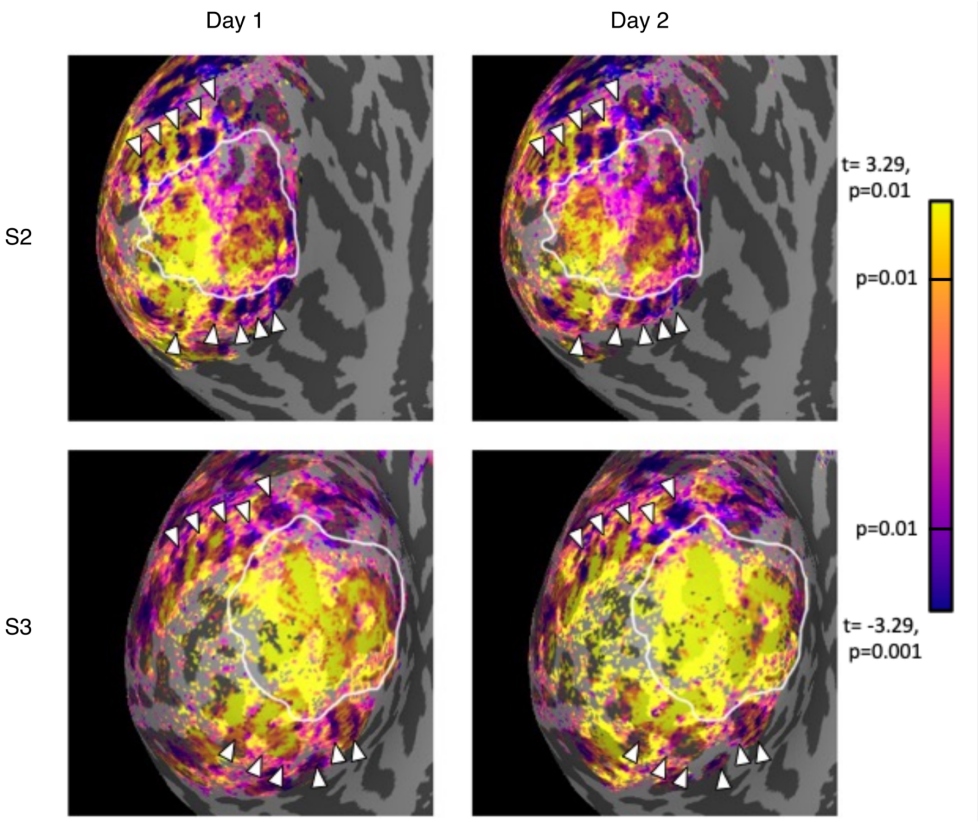

Figure 6. Repeatability of extrastriate bands across days for two participants. Each panel shows an inflated representation of the occipital lobe, where dark gray indicates sulci and light gray indicates gyri. The color overlay indicates the t-statistic associated with the chromatic-achromatic contrast is significant ($p < 0.01$, uncorrected). Yellow nodes represent significant chromatic selectivity and purple nodes represent significant achromatic selectivity. White arrows point to achromatic stimuli-selective bands that are consistent in location across days.

4. Discussion

In this work, we examined whether selectivity for slow-flickering, chromatic stimuli varied through the cortical depth. We found that responses to chromatic stimuli were larger than responses to achromatic stimuli in superficial GM, but not deep GM, even after normalizing by average percent signal change to account for superficial bias in T2∗weighted fMRI. This finding suggests that the underlying laminar profile of responses to chromatic stimuli is biased toward superficial layers, compared to the underlying laminar profile responses to high-contrast achromatic stimuli. This finding is consistent with a preliminary result previously found in humans (Olman et al. 2012).

One possible explanation for the apparent superficial bias for responses to the chromatic stimulus, relative to the achromatic stimulus, would be the location of cytochrome oxidase (CO) blobs to which color sensitive neurons project. Those blobs are most evident in superficial layers 2 and 3 (Horton, 1984), and weakly present in deep layers 5 and 6 (Livingstone and Hubel, 1982). The superficial CO blobs sit higher in the GM than the Layer 4B neurons that are the primary V1 target of the M pathway neurons (in NHP) and are expected to respond more strongly to the achromatic stimuli than the chromatic stimuli.

The pial bias of the BOLD signal in superficial layers is a known challenge for depth-dependent analysis of GE data in particular (Uludağ & Blinder, 2018). To account for this, we took careful steps to minimize the possible influence of large surface vessels by removing voxels that had (vein-attributed) high SNR from analysis and normalizing activation differences at each depth by overall activation levels to verify that the P-

selectivity in superficial layers was due to the stimuli and not an artifact due to the location of select voxels. Normalization, in particular, removes a significant portion of the superficial bias known to be present in the fMRI signal, but not all of it. The strongest evidence that the pial bias in chromatic selectivity is not merely an artifact of the imaging modality is that it varies with eccentricity throughout V1.

Another caveat for interpretation of the measured bias toward chromatic stimuli in superficial layers is that superficial signals can represent signals from middle and deep layers (Havlicek & Uludağ, 2020). It is possible that the bias is actually present in middle layers, but upward pooling of fMRI signal extends the bias to superficial layers. However, a superficial signal that is only inherited from deeper sources would not be larger than a signal in deeper sources, as we see in our data (Figure 5), particularly in middle and peripheral ROIs. Thus, despite not including a depth-deconvolution step (Havlicek and Uludağ, 2020) by subtracting deep signals from middle signals in our analysis, we conclude that the positive bias in superficial layers in our data is a result of chromatic selectivity.

In addition to observing chromatic selectivity (preference for chromatic stimuli compared to achromatic stimuli) across depth, we also examined how chromatic selectivity varied with eccentricity. We found that parafoveal regions were more responsive to chromatic stimuli than achromatic stimuli, and peripheral responses to chromatic and achromatic stimuli were similar. Interestingly, the variation in chromatic selectivity was due to differences in achromatic responsivity: responsivity to red/green slow-flickering (0.5 Hz) stimuli was roughly constant across the visual field, and

responsivity to achromatic, fast-flickering (12 Hz) stimuli increased with eccentricity. This result diverges somewhat from a demonstration of eccentricity dependence of temporal frequency sensitivity, where sustained flicker responsivity (roughly associated with the P pathway) declined with eccentricity, and transient flicker responsivity (roughly associated with the M pathway) was roughly constant across eccentricity (Horiguchi et al., 2009). However, our data are consistent with findings from a 3T fMRI study showing achromatic responsivity as relatively constant near the vertical meridians in V1 and increasing across the visual field along the horizontal meridian (Vanni et al., 2006). Our stimuli and ROIs avoided the vertical meridian, which maximized our sensitivity to this previously reported increase in responses to achromatic stimuli with increasing eccentricity. Responsivity to chromatic stimuli was roughly constant across eccentricity in our data, which is consistent with fMRI results showing red/green modulation to be evenly distributed up to 20° eccentricity when stimuli are corrected for cortical magnification (Vanni et al., 2006).

Our chromatic stimulus was not corrected for varying isoluminance values across eccentricity. The isoluminance point varies somewhat with eccentricity (Bilodeau & Faubert, 1997; M. S. Livingstone & Hubel, 1988; Mullen, 1985); however, this variation (~5% increment or decrement in effective contrast over the central 20° of the visual field) is relatively small compared to the changes we measured with eccentricity. The variation in the isoluminance point across eccentricity likely contributed to the degree to which our chromatic stimuli evoked neural responses; however, we do not believe the spatial variation in isoluminance point across the visual field is enough to explain an increase responsivity to chromatic stimuli in regions beyond 10° eccentricity. A follow-up study controlling for the isoluminance variation would rule out this possible confound.

Our third finding was the expression of alternating, repeating bands of chromatic or achromatic selectivity stemming from the V1 border into V2 and V3. In multiple participants, we found chromatic and achromatic bands for both the dorsal and ventral sides of V1. In general, the bands in our data followed a pattern similar to bands described in past fMRI studies that concluded these alternating bands of activation were analogous to those found in functional imaging studies that used chromatic and achromatic stimuli (Nasr et al., 2016; Tootell and Nasr, 2017) or stimuli manipulating temporal frequency (Dumoulin et al., 2017). These bands were consistent in size and found across days for various participants. We characterized the size and pattern of these bands to understand if the patterns in our data entailed a similar kind of marker for color selectivity. The spacing between our bands was on the larger range previously reported averaging ~7.7 mm distance from the center to center of adjacent bands of the same type (e.g. thick-thick) compared to a 4–8 mm range distance reported in humans (Adams et al., 2007; Burkhalter & Bernardo, 1989; Dumoulin et al., 2017; Hockfield et al., 1990; Nasr & Tootell, 2018; Tootell & Nasr, 2017; Tootell & Taylor, 1995). This is expected, since the smaller end of that range comes from postmortem studies, and tissue contraction during histological preparation is expected. Furthermore, we found that the expression of these bands was stable across multiple days of scanning (Figure 6).

The widths of the chromatic-selective and achromatic-selective bands in V2 of our study were roughly comparable. This finding is in line with studies reporting variable widths of thin/thick stripes in macaques (Hubel and Livingstone, 1987; Li et al., 2019; Roe and Ts'o 1997). The bands in our study are defined by the subtraction of two competing conditions, rather than isolated presentation of a single condition; therefore, the width of

the bands will be determined by the relative strength of the stimuli in activating the different populations of neurons in the corresponding bands. Our stimuli were presented dichoptically, which would produce suboptimal responses in the stereo-selective thick V2 stripes (assuming human anatomy matches NHP anatomy) and reduce their apparent width. While the presence and color-selectivity of alternating bands suggests strong similarities between human V2 physiology and NHP physiology, our fMRI study, using differential methods cannot make specific claims about the relative widths of the bands in V2.

Our data join the ranks of about a dozen other datasets that test submillimeter fMRI against known underlying mesoscale neural architecture and conclude that fMRI, if used carefully, has the spatial specificity to distinguish the responses of neuronal responses separated by less than a millimeter. Previous work also showed, however, that if care is not taken in developing laminar profiles, errors are easily made in assigning depth to functional responses or interpreting depth-dependent profiles. Our analysis pipeline included steps that excluded regions where accurate alignment cannot be verified (Weldon et al., 2019) or where the presence of surface veins biased laminar profiles (Kashyap et al., 2018; Olman et al., 2010). The key to our ability to study the eccentricity dependence of M/P laminar profiles was using a T1-weighted EPI (van der Zwaag et al., 2018) to guide non-linear registration between functional and anatomical data across the entire area of the primary visual cortex. The functional data themselves do not have good enough contrast between GM and WM to guide non-rigid-body warping, and rigid-body warping can only optimize registration for a subset of the functional volume when significant distortions are present (distortion compensation from fieldmaps can be

applied but is never perfect). With this addition, however, we were able to generate laminar profiles across an extended region of interest with good confidence in their accuracy, because the segmented T1-weighted EPI also allowed computation of a metric of local registration quality (GM Overlap). This work has therefore demonstrated that sub-millimeter fMRI techniques are now robust enough to pursue large-scale depth profiling of cortical responses.

We used the neuroimaging tools developed in this study to continue exploring visual properties of the primary visual cortex. This led us to our next study on orientation tuning and orientation preference of voxels from the primary visual cortex at the meso-scale.

Chapter 2: Orientation Selectivity in Visual Cortex Using Ultra-High Field fMRI

1. Introduction

Since discovering orientation selectivity in cortical neurons in cats (Hubel & Wiesel, 1959), researchers have been interested in quantifying the selectivity and distribution of orientation tuning in humans. This has proven to be a difficult task since these properties cannot be derived from human histology. Therefore, a large part of our knowledge comes from animal electrophysiological studies. Previous studies have captured fine-scale characteristics of orientation tuning (i.e., orientation selectivity and orientation columns) in non-human animals and coarse-scale characteristics (i.e., distribution of orientation preference) in humans. The present study used high-resolution fMRI to characterize the spatial distribution of orientation selectivity and orientation preference in the human primary visual cortex. High-resolution fMRI is an *in vivo* method with the resolution to examine layer-specific differences in selectivity, a capacity that was previously unattainable with non-invasive imaging methods.

Orientation selectivity is quantified by tuning curves that describe neuronal response vs. stimulus orientation. A neuron with high selectivity will have a sharp response peak at its preferred orientation and weak responses at flanking orientations; a neuron with weak selectivity will have a wider response peak. In non-human animals, neurons vary in how selective they are to a preferred orientation (Chen et al., 2005; Okamoto et al., 2009; Ringach et al., 2002) and how selective a neuron is to its preferred

orientation can change across V1 layers (Cho et al., 2022; O'Herron et al., 2016; Ringach et al., 2002; Van Hooser et al., 2013).

Animal studies using optical imaging and electrodes have found that neurons in superficial and deeper layers of V1 have higher orientation selectivity than middle (input) layers (O'Herron et al., 2016; Ringach et al., 2002; Van Hooser et al., 2013). Recently, this pattern was found using high-resolution fMRI for cat area 18 (Cho et al., 2022). This property has been captured in animals, but it is unclear if it is similar in humans. Orientation selectivity is dynamic and can be influenced by the visual stimulus presented. For example, adding a stimulus outside a neuron's receptive field at the same orientation as the receptive field can suppress the neuron's firing rate (Schwartz et al., 2007). This kind of suppression can cause a sharpening of the tuning width, meaning orientation selectivity increases (Chen et al., 2005; Ringach et al., 2003). Both feedforward and feedback processes can affect orientation selectivity, which is likely generated by the enhancement of the preferred orientation and suppression from cortical inhibition in neurons (Chen et al., 2005; Serences et al., 2009; Shapley et al., 2003).

The orientation preferences of neurons tend to organize in predictable patterns. Neurons with similar orientation preferences tend to cluster together across space and depth (Ohki et al., 2006). Across the cortical surface, neurons tend to cluster in repeatable pinwheel-like patches that change orientation preference gradually around a center, either clockwise or counterclockwise (Blasdel & Salama, 1986; Bonhoeffer & Grinvald, 1991; Braitenberg & Braitenberg, 1979; Kaschube et al., 2010; Ohki et al., 2006). These pinwheels repeat across the cortex, creating column orientation maps (Bonhoeffer & Grinvald, 1991; Hubel et al., 1978; McLoughlin & Schiessl, 2006; Singer, 1981; Yacoub

et al., 2008). These columns have been found to be around 0.5 mm in width for carnivores (Bonhoeffer & Grinvald, 1991) and are estimated to be around 0.8 mm in humans (Yacoub et al., 2008).

Only one study on humans has been able to capture orientation columns at a fine-submillimeter scale due to limitations in the spatial and temporal resolution of the imaging methods available (Yacoub et al., 2008). However, these methods have captured coarse-scale distributions of orientation tuning in V1 (Freeman et al., 2011; Furmanski & Engel, 2000; Mannion et al., 2010; Roth et al., 2022; Sasaki et al., 2006, 2006; Sun et al., 2013). For example, fMRI studies have shown that voxels that display orientation preferences demonstrate a radial bias where the preferred orientation of these voxels points towards fixation; this bias demonstrates a relationship between retinotopy and orientation preferences in V1 (Freeman et al., 2011; Larsson et al., 2017; Mannion et al., 2010; Roth et al., 2022; Sasaki et al., 2006). Other studies have found another distribution called the oblique effect, where more voxels prefer vertical and horizontal orientations (Furmanski & Engel, 2000; Sun et al., 2013).

With the rapid advances in high-resolution fMRI, we can image at resolutions that allow direct detection of columns (Yacoub et al., 2008) and inference of information flow through cortical layers (Huber et al., 2017; Kok et al., 2016; Navarro et al., 2021; Olman et al., 2012; Uğurbil et al., 2003). The present study was conducted to determine whether we could (1) detect changes in orientation selectivity through depth, (2) determine whether large-scale distribution of orientation preference matches coarse scale distributions captured in previous studies (i.e., radial bias, oblique effect), and (3) detect a pinwheel-like pattern of orientation columns.

2. Methods

2.1 Participants

Seven neurotypical adults (five females) aged 23 to 48 years old participated in the experiment. All experimental procedures were approved by the University of Minnesota's Institutional Review Board. Written informed consent was obtained from all participants before the experiments under the Declaration of Helsinki. Participants were compensated at a rate of $20 per hour.

2.2 Apparatus

The stimuli were presented using an NEC NP4000 projector with an effective frame rate of 60 Hz. Participants viewed the stimuli through a mirror which was placed approximately 15 cm from the participant's eyes and 65 cm from the projector screen for a total path length of 80 cm from the projected image to the participants' eyes. Projections spanned a 42 cm x 31.5 cm rectangular space on the projector screen.

2.3 Experimental Design

2.3.1 Visual Stimuli Stimuli were generated using PsychoPy (Peirce et al., 2019). All stimuli were composed of sine-wave gratings with a spatial frequency of 1.6 cycles/degree and 40% contrast. Stimuli were divided into three sub-regions, a circular spatial surround subtending 25^{o} of visual angle and centered at the fixation, two circular target regions subtending 2.5^{o} of visual angle placed at 3^{o} eccentricity and rotated 30^{o} below the horizontal meridian with one target on each side of the vertical meridian, and an open white circle centered on fixation subtending 1.25^{o} of visual angle (Figure 7).

Grating stimuli were presented at 1 of 8 orientations, ranging from 0° to 180° in steps of 22.5°.

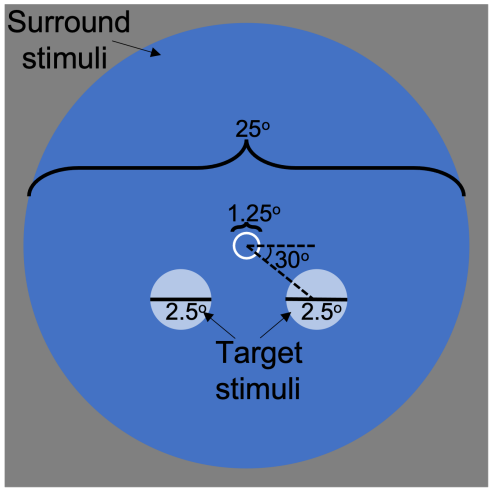

Figure 7. Stimulus spatial configuration. Surround stimuli subtended 25° of visual angle. A central white outlined circle was positioned at fixation and subtended 1.25°. Target stimuli subtended 2.5° and were placed and rotated 30° below the horizontal meridian.

Each trial lasted 1.2 s. First, both surround and target stimuli were presented simultaneously for 250 ms. This was followed by a gray screen for 200 ms. Next, the stimuli were presented again for 250 ms but shifted clockwise or counterclockwise. The size of the shift was controlled according to a three-down, one-up staircase method (Taylor & Creelman, 1967) with a list of possible orientation shifts of 1°, 2°, 3°, 4°, 6°, 8°, 12°, and 16°. This was followed by a gray screen for another 300 ms. The participant was allowed to respond as soon as the shifted stimuli were presented for a response window of 500 ms. For the remainder of the trial (200 ms), feedback was provided by changing the outline color of the circle at fixation to green or red for correct or incorrect responses, respectively (Figure 8). The participant's task was to report if the stimuli in the second presentation were oriented clockwise or counterclockwise with respect to the initial

presentation. Each trial was jittered by 300 ms intervals so that a trial could begin immediately after the previous trial, 300 ms, or 600 ms after.

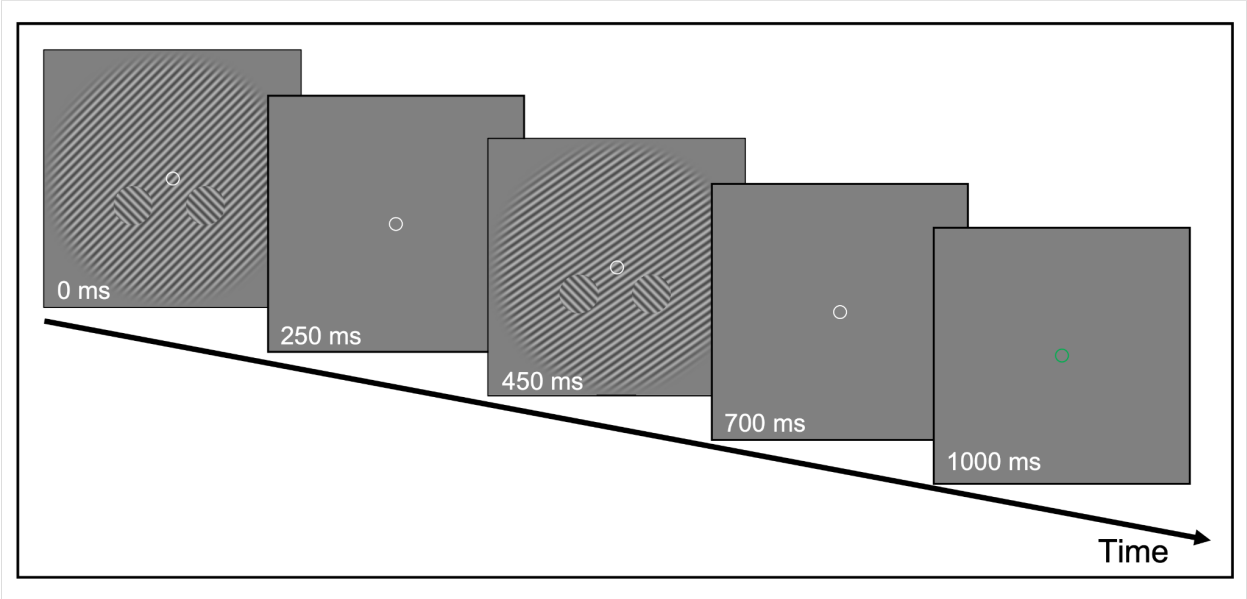

Figure 8. Single-trial timeline. A single trial lasted 1.2 s. The stimuli were presented for 250 ms, followed by the interstimulus interval where a gray screen was presented, which lasted 200 ms. The stimuli were then presented again but shifted clockwise or counterclockwise for 250 ms; at this point, the response window started. This was followed by an interstimulus window that averaged 300 ms. Feedback was then provided by changing the color of the center circle to indicate correct or incorrect judgment, which lasts 200ms.

A single block consisted of 8 trials. The average orientation of each pair of stimuli was the same for an entire block. Only one condition (defined below) was presented per block.

2.3.2 Experimental conditions The experiment was divided into two types of functional scans: task scans and localizer scans. Task scans contained a rest condition and four visual conditions presented in a blocked design: surround-only, iso90, orth, and iso. During rest, no surround or target gratings were presented. Instead, there

was only a grating within the white outlined circle at fixation. In the orth condition, the target gratings had the same phase as the surround grating, but their orientation was orthogonal to the surround grating. In the iso condition, the target gratings were presented with the same orientation and phase as the surround grating. In the iso90 condition, the target gratings had the same orientation as the surround grating but with a relative phase shift between the two of 90°. In the surround-only condition, the target gratings were omitted and replaced with gray circles that matched the luminance of the background (Figure 9A).

All conditions, including rest blocks, were presented eight times in pseudorandom order within one task scan, once at each of the eight possible orientations. Each block was 12 s, so a single scan lasted 480 s. A total of four functional task scans were conducted during a session (Figure 9B).

The second kind of functional scan - localizer scans, were used to localize the regions of interest corresponding to the target and surround. Two conditions were used to identify voxels responsive to the target and surround, respectively: a target-only condition and a surround-only condition. In the target-only condition, the surround grating was omitted, and the participant was asked to perform the same two-interval forced-choice orientation discrimination task described above (section 2.3.1) but on the grating within the white circle at fixation (Figure 9C). Target and surround gratings were presented at each orientation from the same set of eight equally spaced orientations from 0^{o} to 180^{o} in random order. The scan lasted 204 s, and each condition was presented for 12 s. Each localizer scan started and ended with a surround block. Blocks alternated between surround and target blocks for a total of nine surround blocks and eight target

blocks (Figure 9D). Due to the extra surround block, one randomly selected orientation was presented during two surround blocks, while the remaining seven orientations were each presented during one block only. All other timing and stimulus parameters remained consistent between task and localizer scans. A total of three localizer scans were conducted during each session, except for one session, where only two localizer scans were collected due to time restrictions.

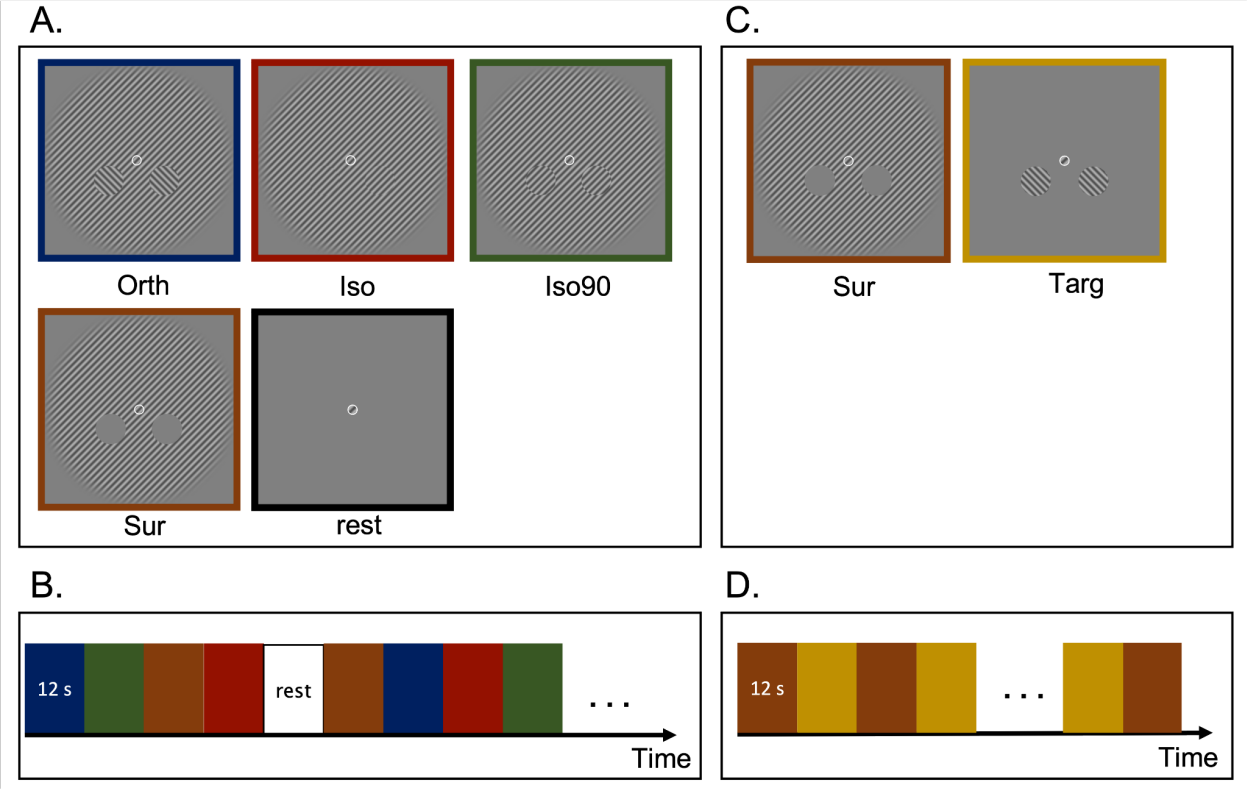

Figure 9. Visual conditions and block structure for task and localizer scans. A) Visual conditions for the functional target task. Depending on the condition, two target stimuli were presented below the horizontal meridian. The average orientation of the target (and surround) stimuli was systematically varied. See text for descriptions of specific conditions. B) Block design for the task scans. Each condition was presented pseudo-randomly for 12 s, followed by 12s rest. C) Visual conditions for the localizer scan. See text for descriptions of specific conditions. D) Block design for the localizer scan. The scan started and ended with the surround-only condition.

2.4 Data collection

Functional MRI data were collected at the University of Minnesota's Center for Magnetic Resonance Research on a Siemens 7T scanner equipped with a custom-made head coil (32-channel transmit, 4-channel receive) (Adriany et al., 2012) that was used for T_2*-weighted gradient echo (GE) echo-planar imaging (EPI). Images were acquired with a coronal orientation in 25 slices positioned to capture the posterior extent of the occipital lobe. Image resolution was 0.6 mm isotropic (field of view (FOV): 124.8 mm x 153.6 mm; matrix size: 208 x 256); the data were acquired with an in-plane parallel imaging acceleration factor (R) of 3 using GRAPPA (Griswold et al., 2002) and a right-left phase-encode direction (6/8 Partial Fourier, echo-spacing: 0.12 ms). The repetition time (TR) was 2 s, and the echo time (TE) was 32.2 ms.

During each scanning session, we acquired (1) Two additional T_1-weighted GE EPI (T_1wEPI) sequence scans used to define the gray matter (GM) in the functional data (van der Zwaag et al., 2018), one with a reverse phase encode direction. Since both the T_1wEPI and the functional data were collected in the same session with the same resolution, sampling, and echo spacing, they were subjected to the same distortion and provided a more accurate GM delineation. (2) We acquired an additional 7T anatomical scan during the session as a T1-weighted MP-RAGE (0.5-mm isotropic, TR = 6000 ms, TI = 1200 ms, TE = 3.58 ms, flip angle = 8°, FOV = 192 x 192 mm). This scan provided enhanced myelin visualization (Fracasso et al., 2016).

An additional T1-weighted MP-RAGE scan (0.8-mm isotropic) was also separately acquired on a Siemens 3T scanner. All participants completed a separate retinotopic mapping scan at 3T (2 participants) or 7T (5 participants). The visual stimuli displayed

were either oriented moving bars used to fit a population receptive field model (pRF) (Dumoulin & Wandell, 2008) or wedges/rings used to stimulate receptive fields at varying eccentricities and create retinotopic maps from the fMRI signal response (Engel et al., 1997). Both types of retinotopic mapping were used to define V1/V2/V3 boundaries.

2.5 Data pre-processing

2.5.1 3T data We segmented the 3T reference anatomy to define the GM/white matter (WM) boundary and the pial surface using FreeSurfer's `recon-all -hires -expert` command by inflating the cortical surface for a max 100 iterations (https://surfer.nmr.mgh.harvard.edu/, v6.00.0).

2.5.2 NOise Reduction with DIstribution Corrected (NORDIC) PCA NORDIC is an algorithm for reducing thermal noise in functional (Vizioli et al., 2021) and diffusion-weighted (Moeller et al., 2021) MRI, which at high resolution is the dominant source of noise. We applied this algorithm to our raw functional data, prior to any other preprocessing, to improve our SNR, which increased by a factor of 2.

2.5.3 Functional data Functional data were processed using tools provided by AFNI (https://afni.nimh.nih.gov/afni, v22.0.10). Motion compensation was performed using AFNI's `3dvolreg` command on all functional data registering to the forward phase T1wEPI. Motion compensation was done in two steps: within and between functional scans. The mean of each scan was registered to the T1wEPI before within-scan compensation was done, providing higher SNR.

The voxel displacements required to un-distort the functional data were estimated with `3dQwarp` using both forward and reverse T1wEPI. The WARP volume was then

combined with the motion correction parameters to produce a single re-sampling matrix used to apply motion- and distortion correction to the functional data in one step to reduce image blurring due to interpolation.

After performing distortion compensation on the two T1wEPI scans and averaging together, we processed the data from the T1wEPI by fitting each voxel's intensity as a function of the slice-specific inversion time for each volume acquisition. These fits provide an image with T1-weighted contrast, which we then used as the target for 3T anatomy alignment to bring the high-quality anatomical image into functional space using `3dAllineate`. We also used this process to align the T1wEPI to the 7T anatomy. The anatomy was resampled to functional space since the scan has a higher resolution.

2.6 Data Analysis

2.6.1 General linear model (GLM) analysis The data were analyzed with a standard general linear model (GLM) using AFNI's `3dDeconvolve`. Stimulus regressors were boxcar functions convolved with a hemodynamic response function [hrf = tˆ4∗exp(-t)/(4ˆ2∗exp(−4)] with the timings of each boxcar matched to the onset of the stimulus blocks. The design matrix also included nuisance regressors for baseline drift (Legendre polynomials out to the fourth order) and motion (estimated from AFNI's `3dvolreg`). Beta weights were estimated with the ordinary least squares solution to the GLM. Three GLMs were conducted. For the localizer scans, a GLM was constructed with a design matrix that included regressors for target-only (Targ) and surround-only (Sur) conditions used to

define our ROIs. Two orientation GLMs estimated the response amplitude for each of the eight tested orientations for the surround and target stimuli. The surround GLM used localizer and task scans (7 scans total), and the target GLM used only the task scans (4 scans total). Voxels not significantly modulated by visual stimulus presentation ($p < 0.01$, were excluded from further analyses.

2.6.2 Target ROI delineation The resulting polar angle retinotopic maps were used to verify and manually refine V1, V2, and V3 boundaries defined by a publicly available atlas (Benson et al., 2014). Retinotopically defined V1/V2/V3 ROIs were aligned and resampled to the in-session T1wEPI from 7T using AFNI's `3dAllineate`. We used the functional localizer scan with target-only and surround-only conditions to identify voxels responsive to the target and surround by running a GLM (defined above 2.6.1) with regressors for target-only and surround-only conditions. We then thresholded voxels significantly modulated by the target stimuli ($p<0.001$) (Figure 10A).

Using the V1 boundary and the localizer scan as a guide, a center point for a target-selective ROI was visually estimated. We wrote a custom Python algorithm to select the surface nodes within a 10mm radius of this center point and created a flat patch (Figure 10A). The patch was visually inspected to ensure all voxels activated by the target stimuli were included. The surface patch was then translated to a volume in the functional space using AFNI's `3dSurf2Vol` by using the depth segmentation from the 3T anatomy and assigning each voxel in functional space the surface node value with the most significance. Finally, we used the flattened cortical space defined by this patch to fit an elliptical boundary to target-selective voxels within the 10mm radius using the principal components of the voxel locations in 2-dimensional surface space as the major and minor

axes (Figure 10B). This provided two advantages: 1) a more precise localization of the boundary between target-selective and surround-selective voxels, and 2) a measure of radial distance from the center of the target-selective region to the edge of the boundary for each voxel. We found that the optimal boundary between target- and surround-selective voxels occurred at about two standard deviations of the 1st and 2nd principal components. This boundary defined our target ROIs. An ROI was drawn in each hemisphere of every participant except for one where the localizer could not significantly distinguish between target and surround for a total of 13 ROIs.

Non-target ROIs were drawn in regions that mirrored the target ROIs over the horizontal meridian. However, ROIs were only drawn on hemispheres with enough space between the target ROI and the V1 border, which totaled seven ROIs. These regions were meant to capture activation to the surround stimulus at the same eccentricity as the target ROIs. Like in the target ROIs, a center point was visually estimated using the target ROI and the V1 boundary as a guide. From this center point, a 10 mm radius was created. We did not conduct our PCA estimation since this region had no stimulation. Instead, only voxels within a 5 mm radius of the ROI were considered in analyses to match the size of the target ROI and avoid overlap in voxels within the two ROIs.

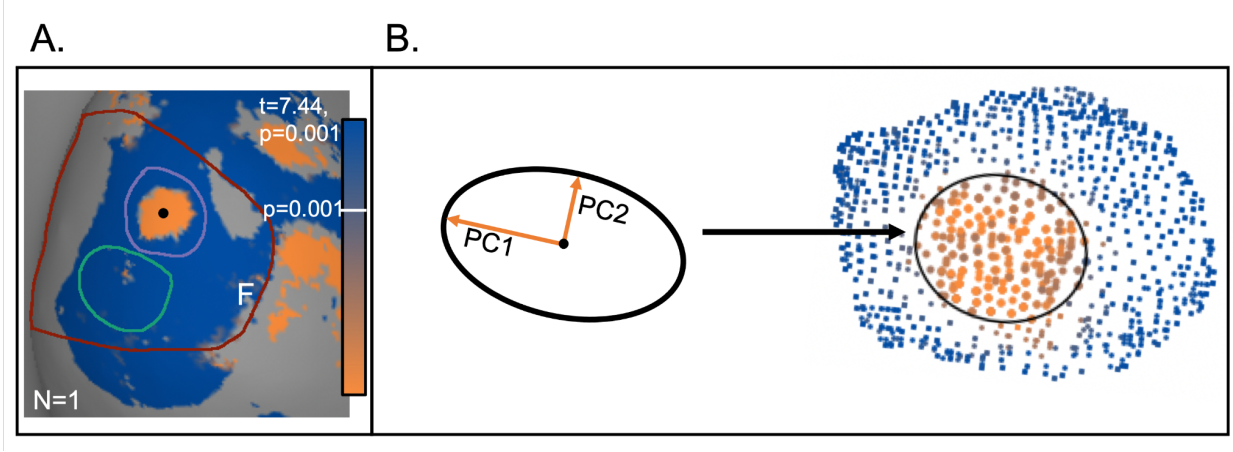

Figure 10. Target ROI delineation. A) T-statistics for the Fourier localizer displayed for one participant on an inflated representation of the occipital cortex on the right hemisphere. Surface nodes with significant responses to our target stimuli are in orange ($p<0.001$). The fovea is labeled with the letter "F". The purple border indicates the area where a target patch would be drawn, and the green border indicates the non-target patch. The red border is the V1 boundary. The center of the target ROI is estimated visually, denoted by a black point. B) An elliptical boundary is created using PCA to classify all activated voxels for the target stimuli in the flattened cortical space. This boundary was then used to define the target ROI (black line).

2.6.3 Depth-dependent analysis Cortical layers were defined by segmenting the GM derived from the 3T anatomy into 20 depths using an equivolume solution on surface space (Waehnert et al., 2014) using FreeSurfer (https://github.com/kwagstyl/surface_tools). These depth-dependent meshes were then projected into the functional data space. Each voxel was assigned a depth depending on where the voxel is registered on the surface segmentation in the anatomical GM from the white matter surface to the pial surface. Only voxels that met the inclusion criteria (discussed in section 2.6.5) and were within the target and non-target ROIs, respectively, were considered. Depth-dependent fMRI profiles were formed by averaging functional responses in 6 depth bins ignoring any voxels with a depth assignment closest to the WM or the pial surface. Statistical analysis was conducted with Python.

2.6.4 Orientation preference estimation The orientation preference of each voxel was estimated by fitting tuning curves to the beta weights obtained from the surround and target GLMs at the eight tested orientations. The response for each orientation in each voxel was then fit using the von Mises function, resulting in four fitting parameters from the following formula (Swindale, 1998):

$$O(\theta) = A \cdot e^{k(cos(2(\theta-\theta p))-1} + B$$

here O is the response of the model, theta (θ) is the orientation of the stimulus, θp is the orientation at which the response is maximal. this parameter was used to define the preferred orientation of each voxel for analysis of orientation preference distribution in V1. Parameters A and B are scaling parameters for the curve.

The orientation selectivity index (OSI) was used to determine how tuned a voxel is to its preferred orientation(Cho et al., 2022; O'Herron et al., 2016; Ringach et al., 2002). OSI is 1- circular variance therefore, an OSI close to 1 means the voxel is highly tuned toward its preferred orientation. OSI was calculated as follows:

$$OSI = abs\left[\frac{\Sigma_k r_k e^{i20k}}{\Sigma_k r_k}\right]$$

here r_k is the averaged response which for this study refers to the beta weight obtained for each orientation. Voxels with negative responses were not fit. OSI values of voxels positioned at each of the six depth bins for each ROI were averaged and plotted.

2.6.5 Inclusion criteria All ROIs included in the final analysis had a temporal SNR (tSNR) higher than 11 after distortion compensation. We only included ROIs with more than 50% of significant voxels modulated for visual presentation at a significance

level of $p<0.01$. As a result of these inclusion criteria, we included 15 ROIs in five out of seven participants for our statistical analysis. Nine of the datasets were target ROIs, and six were non-target ROIs. After the voxels in each ROI were fit using the Von Mises function (as described in 2.6.4), we calculated a goodness-of-fit value (R^2). Only significantly modulated voxels with an $R^2 > 0.5$ were considered in subsequent analyses. For depth-dependent analysis, we used one more criterion to ensure each depth had enough voxels for analyses. All voxels within a dataset were binned into three depths. Each dataset needed to have at least 20 voxels in each binned depth. This results in 10 of the 15 ROIs to be included in this analysis.

3. Results

In general, OSI values ranged between 0.1 and 0.2, values similar to those found previously in cats using hemodynamic measures (Cho et al., 2022; O'Herron et al., 2016). On average orientation selectivity was higher in deep layers (Figure 11). Deep layers had a mean OSI of 0.16 +/- s.e.m. 0.02, middle layers had a mean OSI of 0.14 +/- s.e.m 0.02, and superficial layers had a mean OSI of 0.15 +/- s.e.m 0.02. A one-way ANOVA was conducted that examined the effect of depth on average OSI values. There was no statistically significant effect of depth on OSI, $F(2, 27) = 1.55$, $p = 0.23$. We also conducted some planned comparisons on OSI across depth. We conducted three separate one-sample t-tests to understand if the difference between layers differed significantly from zero (Figure 5B). We found a significant difference between deep and middle layers ($t(9)=5.24$, $p< 0.001$) and deep and superficial layers ($t(9)=2.65$, $p=0.011$).

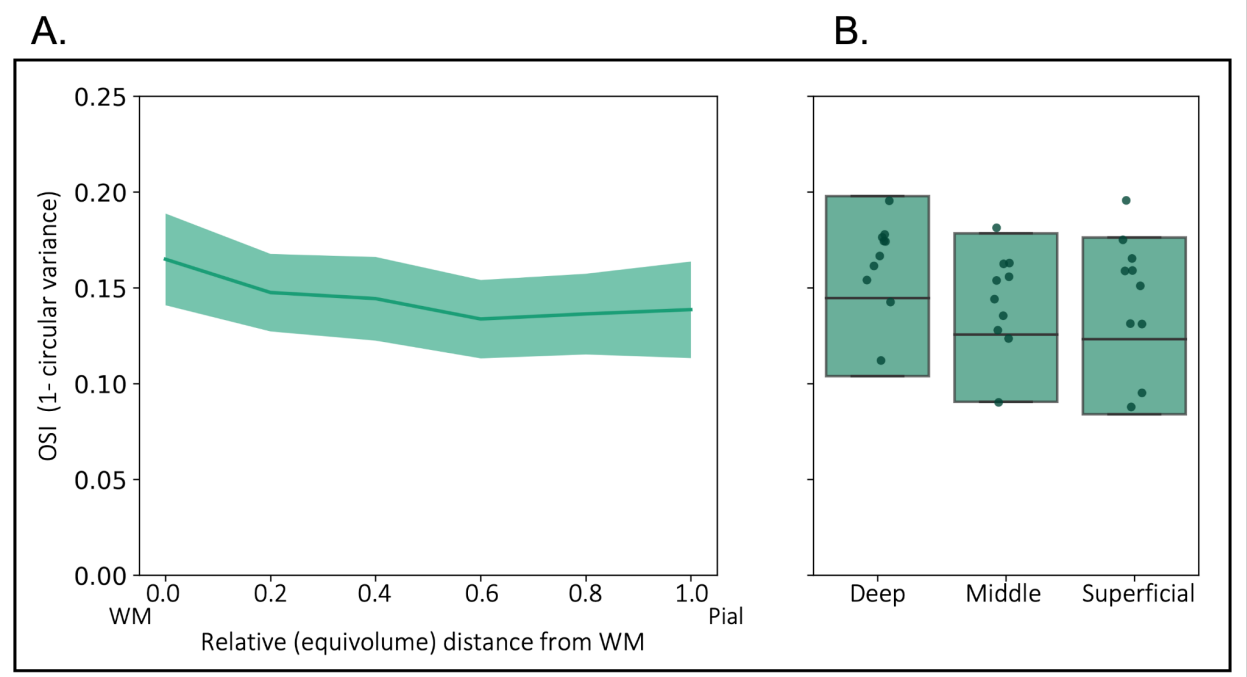

Figure 11. Orientation selectivity across depth in V1. A) Estimates of the OSI values averaged across depth. Data represent OSI values from four target ROI and six non-target ROI datasets meeting all inclusion criteria; shading indicates standard error of the mean. B) The same data as in (A) binned into the three depths used for statistical analysis. The shaded area in each box represents the first quartile to the third quartile with the horizontal line inside the box representing the median. Single points indicate mean OSI values of individual datasets.

We also observed radial bias in our data. The distribution of orientation preferences within each ROI was not uniform and peaked around a mean polar angle (Figure 12A, B). To check if the distribution of orientation preference was uniform for any of our ROIs, we conducted a Watson's Test for Circular Uniformity. This test demonstrated that none of our ROIs were uniformly distributed. Therefore, we moved forward with testing if the mean orientation preference in each ROI was reliably around the same retinotopic location (Figure 12C). To do this, we conducted a circular statistics test that could properly capture the concentration of the angles around a mean. We were interested in understanding if the direction of the mean resultant vector was similar

between orientation preference and the polar angle within each ROI. We conducted Rao's test for equality of polar vectors, which has been shown to perform well at controlling type I errors (Landler et al., 2021). We found that there was homogeneity of polar vectors in 5 out of 10 of our ROIs with p >0.05. This means that in those ROIs, the mean orientation preferred and polar angle was not significantly different from each other. Orientation preference distributions are skewed toward the polar angle in these ROIs. These results indicate that the measured orientation preference distribution follows a radial bias pattern in half of our ROIs. Three of the remaining ROIs had orientation preference distributions that visually displayed radial bias, but the mean was deemed different from the polar angle mean. The remaining two had an orientation preference peak at cardinal orientations.

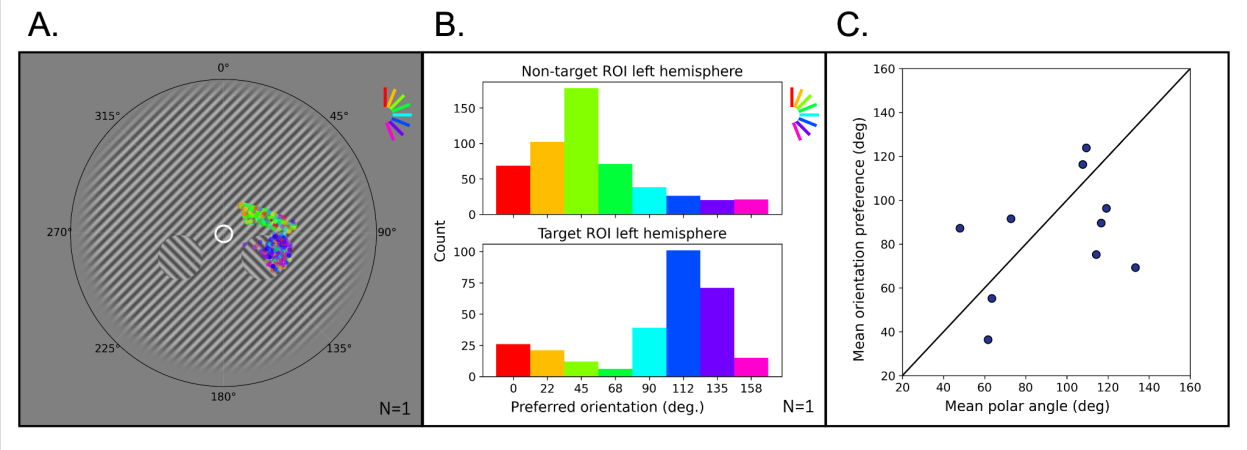

Figure 12. Orientation tuning distributions within the ROIs in V1 and visual space. A) Overlaid are the polar coordinates (from the Benson et al., 2014 atlas) of voxels color coded for their preferred orientations within a non-target ROI and target ROI in the left hemisphere of one participant. Polar coordinates are arranged clockwise, where 0° is vertical. In the background is an example of the visual stimuli presented at the same polar scale. B) The distribution of the orientation preference corresponding to the voxels in the ROIs from A. The skew of each distribution matches predictions from the retinotopic location of the ROI. C) Mean orientation preference vs. mean polar angle for each ROI. The black line is y=x. Points close to the black line have similar mean polar angles and orientation preferences, indicating a radial bias in those datasets.

4. Discussion

We found that the average OSI values (M=0.16) were in line with the work conducted by Cho et al., 2022 who conducted depth-dependent fMRI in cats and found values ranging around 0.1 to 0.2 across layers. Our average values are also in line with previous work that found that imaging methods that measure blood flow, like fMRI, result in lower OSI values (0.2) compared to methods that measure neuron spiking activity because of the dilation sensitivity of vessels (O'Herron et al., 2016). Unlike Cho et al., 2022, we found no significant difference between the superficial layers and middle layers. We did find that the difference between the mean OSI in deep layers and middle/superficial layers was significantly higher than zero.

OSI is an extension of circular variance as it is measured as 1 - circular variance. If a voxel consistently responds highest to one tested orientation and weakly to others, the circular variance in this voxel will be low; therefore, the voxel is considered to have higher orientation selectivity. If a voxel responds equally to a range of orientations, then that voxel has higher circular variance and will therefore have low orientation selectivity. In electrophysiology, OSI is considered inherently robust to noise since it measures the variability in mean responses across the tested orientations (Ringach et al., 2002). fMRI methods are vulnerable to spatial blurring/smoothing, where the information that should be contained in a voxel is blurred around to its neighbors either as a product of resampling during preprocessing or pooling over space due to draining veins. This kind of smoothing can create equal responses for all the tested orientations in a single voxel and can mask the true neural orientation selectivity. Therefore, when OSI is measured in these high-responding voxels, the result will be a low OSI. This creates a predicament about whether

the OSI values we compute are true estimates of orientation selectivity in the underlying neuronal populations or if they are estimates biased by spatial smoothing.

The study by O'herron et al., 2016 compared responses of individual blood vessels to the spiking activity of nearby tissue in a cat's primary visual cortex. They found multiple instances of robust dilation response to a visual stimulus when no spiking response was observed for the same stimulus. This resulted in highly broad OSI values (0.2) for blood vessels compared to spiking activity (0.82). However, regardless of these highly variable results in orientation selectivity, they found an almost 1:1 correlation in preferred orientation responses between the two types of responses. Based on these previous and current results, we conclude that human orientation selectivity can be detected using 0.6 mm T2*- weighted fMRI. Still, this number may not be representative of the true orientation selectivity of neuronal activity but rather of the dilation of blood vessels, which pool signal over several neighboring orientation columns.

Next, we wanted to understand if the increase of orientation selectivity in deep layers was due to more orientation selective voxels in these layers or a by-product of contrast to noise ratio (CNR) across layers. We compared our OSI fits against a null distribution. To do this, a normal distribution of random values that reflect the parameters from the beta weights in our data was created. The null distribution had a mean of 3 and a standard deviation of 3. We fit this distribution using the exact same process as our data (see 2.6.4). We found that the resulting OSI distribution (Figure 13A) was similar to the OSI distribution obtained in our analysis (Figure 13C). We discovered that OSI values are highly sensitive to CNR. A high CNR in a null distribution could be replicated by lowering the standard deviation, which resulted in lower OSI values (Figure 13B). This is

because a smaller difference between the beta weights in a single voxel indicates a less selective voxel for a single orientation therefore, more voxels are assigned a small OSI value. This led us to look at the OSI values of our data as a function of the F statistic extracted from the GLM. As expected, we find that voxels with a higher F statistic have a lower OSI value (Figure 13D). We conclude that it is unlikely that the slight increase in OSI in deep layers is due to higher selectivity in deep layers. It is more plausible that this difference is due to lower contrast-to-noise ratio (CNR) in deep layers due to an upward pooling of fMRI signals from deep to superficial layers (Havlicek & Uludağ, 2020).

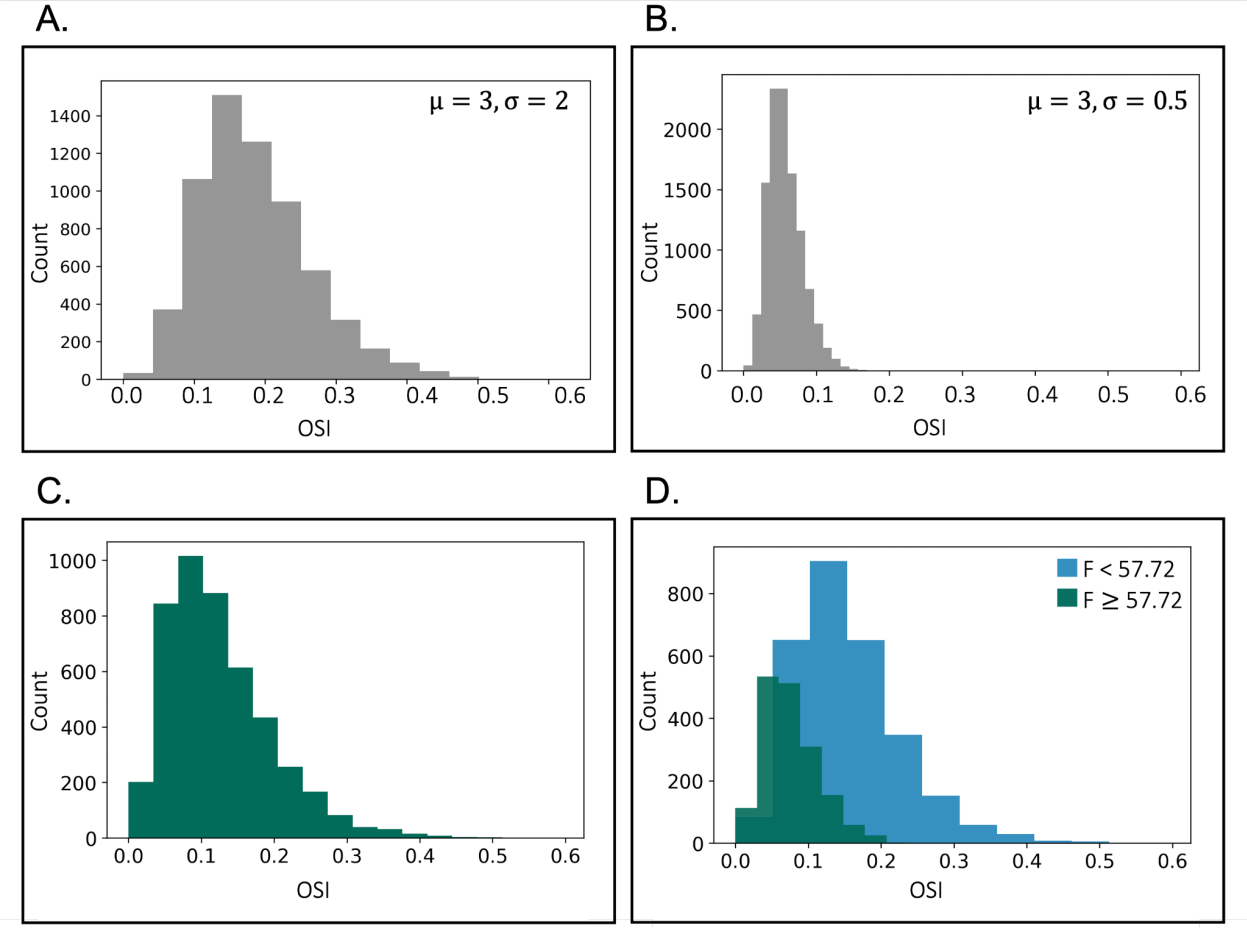

Figure 13. Evaluation of OSI distribution. A) Null distribution of OSI values extracted from a simulation of responses to 8 orientations. The simulated beta weights had the same mean and standard deviation as our data. B) The same null distribution as in (A) but the standard deviation of beta weights relative to the mean is smaller. C) OSI values of all voxels in the datasets included in the formal analysis (10 ROIs). D) The same distribution as demonstrated in (C) (10 ROIs) but separated by voxels with an F statistic greater/lower than the mean F statistic. Voxels with high F statistics have lower OSI values.

In spite of having very weak OSI, the majority of our ROIs demonstrated a reliable preference for orientations based on their retinotopic location, similar to past studies on radial bias, even though we did not capture the entirety of V1 (Freeman et al., 2011; Furmanski & Engel, 2000; Mannion et al., 2010; Roth et al., 2022; Sasaki et al., 2006, 2006; Sun et al., 2013). This bias was seen on both target and nontarget ROIs. Radial bias tends to be more prominent in the periphery (Freeman et al., 2013). Our ROIs were

located around 3° of eccentricity, this is far enough from the fovea to expect strong radial bias across the ROIs. For five of our ROIs, the mean orientation preference was deemed different from its mean retinotopic location. However, in three of those ROIs, we observed an orientation preference distribution approximating radial bias where the spread of orientation preference increased towards the retinotopic location. In one of those five ROIs, we observed a preference for cardinal orientations. In the remaining ROI, we observed a preference for vertical orientations. The variability in orientation preference distributions in our study is consistent with previous observations that a mixture of radial bias and oblique effect provides the best prediction for the distribution of orientation preferences in optical imaging of intrinsic signal in macaque V1 (Fang et al., 2022).

Our data are submillimeter, and therefore, we also conducted a voxel-wise comparison of orientation preference to capture the column-like structures found in previous fine-scale non-human animal studies. This comparison is meant to evaluate the orientation difference between voxels based on their distance from each other inside the ROI. Voxels that are farther away from each other should have larger orientation differences than voxels closer together that are more likely to be inside the same column. However, since the radial bias is inherently tied to the spatial location of each voxel, this was not a feasible approach to capture column-like structures, especially since it is likely that this bias is the dominant signal measured by fMRI (Roth et al., 2018). We plan to repeat this computation by focusing on a voxel's nearest neighbors, looking at the orientation differences between them across cortical space vs. depth. If the distribution displays a column-like structure, the orientation preference should remain unchanged

across depth. Focusing on only neighboring voxels will prevent radial bias from contaminating our analysis.

Chapter 3. Perceptual Learning Can Manipulate Binocular Rivalry Dynamics

1. Introduction

People have two eyes but perceive a single view of the world, formed by combining information from both retinas. Eye dominance is the tendency for information from one eye to be weighted more heavily in determining this perceptual experience (Başgöze et al., 2018; Carey, 2001; Hubel & Wiesel, 1962; Ooi & He, 2020; Tong & Engel, 2001). For example, an object of interest can appear clear, even though the information from one eye is blurry because one lens of the observer's glasses is dirty. This indicates that perception can depend heavily upon one eye, and information from another eye can be discounted or discarded.

Eye dominance is task-dependent, meaning that the weight given to each eye can change with what the observer is doing (Cohen, 1952; Dieter et al., 2017; Ding et al., 2018; Ooi & He, 2020). One commonly studied type is sensory eye dominance which is measured using purely perceptual tasks that estimate the weights given to information from each eye in different judgments. Research conducted over the last few decades has focused on understanding sensory eye dominance.

Binocular rivalry is a perceptual experience that can be used to measure sensory eye dominance. Binocular rivalry occurs when competing stimuli that are difficult to fuse are presented one to each eye, and this creates an alternating perceptual state rather than a fused percept. For example, in a typical rivalry experiment, an observer might be

shown two competing gratings, one at a 45° angle in one eye and the other at a 135° angle in the other eye. In this case, perception alternates between the two stimuli and can correspond to one eye's stimulus for greater amounts of time than the other (Blake et al., 1985; Carey, 2001; Cohen, 1952; Dieter et al., 2017; Ding et al., 2018; Min et al., 2021; Ooi & He, 2020; Qiu et al., 2020). The observer may also experience a mixed percept where both gratings are perceived either as a plaid or a patchwork of each orientation. The time spent between switches is defined as percept durations, and dominance can be measured as the proportion of the total time the stimulus from one eye is exclusively perceived.

Eye dominance is partly determined by situational factors, including the physical properties of the scene being perceived. Changing physical aspects of the target in one eye, such as its luminance, contrast, eccentricity, motion, or other factors, all can affect the amount of time that that eye's target dominates in rivalry (Blake et al., 1985; Brascamp et al., 2015; Sobel & Blake, 2002). For example, if the contrast of one grating is higher than the other, this can cause the observer to perceive that grating for longer periods (Min et al., 2020; Qiu et al., 2020). Some of these factors have been gathered as Levelt's "laws" of rivalry (Brascamp et al., 2015; Levelt, 1965). These laws state, amongst other things, that increasing the stimulus strength for one or both eyes will increase the alteration rate and that increasing the stimulus strength in just one eye will increase the perceived salience but not the average dominance duration of that eye’s stimulus, instead decreasing the duration of the other eye's stimulus.

The state of the observer can also influence eye dominance. This can include attention, fatigue, psychopathology, and even hunger (Chong et al., 2005; Dieter et al.,

2016; Paffen et al., 2008; Weng et al., 2019). For example, in rivalry, if the stimulus in one eye is manipulated in a way that forces the observer to shift their attention to that stimulus over the other, they will perceive the attended stimulus for longer periods (Blake & Logothetis, 2002; Dieter et al., 2016; Lyu et al., 2020; Paffen et al., 2008; Tong et al., 2006; Wang et al., 2021).

Recent work developed a method of changing sensory eye dominance dynamics by training observers to focus on one of two rivaling gratings and manipulating the aspect ratio of that grating (Dieter et al., 2016). In this method, a drifting bull's eye grating is presented to one eye, termed the "trained" eye, and a drifting radial grating is presented to the other eye. While presenting the two gratings, the aspect ratio of the bull's eye grating is gradually stretched to be perceived as a tall or wide oval. Observers were asked to attend to this grating and report the direction of the aspect ratio change over the course of multiple 268 s blocks of stimulus presentation. This training was repeated for 12-24 sessions that lasted between 27-54 min each day. A more typical binocular rivalry task, in which both gratings maintained a circular aspect ratio, was conducted before and after training with the same gratings counterbalanced between the eyes.

Following training, participants spent significantly more time seeing the bull's eye grating when presented to the trained eye than when presented to the untrained eye. This finding suggests that the sensory dominance of the trained eye increased significantly after training. Predominance was so strong that two participants perceived the bull's eye grating 90% of the time during rivalry. This work is promising because it might be used to balance the weights between the eyes of people with severe trait-like eye dominance, such as amblyopia; however, it has yet to be tested on a clinical population.

The current study aims to replicate the findings by Dieter et al., 2016, as a first step in understanding how training on perceptual tasks can change binocular rivalry dynamics; we also want to understand how a mixed perception may influence these dynamics.

2. Methods

2.1 Participants

Six individuals (19–27 years old, mean age: 23 years, 4 female) participated for 13 days each. All participants reported having normal or corrected-to-normal vision. Participants were compensated with $12 per hour for participation. The study was conducted in accordance with the guidelines laid down in the Declaration of Helsinki and approved by the University of Minnesota institutional review board. All participants gave written informed consent before the start of the experiment.

2.2 Apparatus and stimuli

Participants sat in front of a table with their heads supported by a chin rest. Directly in front of them was a mirror stereoscope where the edge mirrors were placed 8 cm away from the center mirror at a 45 deg angle. The edge mirrors were slightly adjusted in angle by the participant at the start of each session by doing a nonius line task where two vertical lines were placed above or below the horizontal meridian and in the middle of the left or right of the screen. The participant was asked to adjust the mirrors accordingly until the two lines merged and they could only see one vertical line in the center of the screen. The total viewing distance from the observer's eyes to the screen, including the distance between the mirrors in the stereoscope, was 68 cm. The stimuli were displayed on an

external display with 1920 x 1200 resolution. The experimental program was written in PsycoPy v2022.2.3 (Peirce et al., 2019). For all tasks, the participant responded using the arrow keys on the keyboard (Apple Magic Keyboard).

Observers viewed two orthogonal gratings: a bull's eye grating and a radial grating (Figure 14A). Both gratings reversed their contrast at 1.5 Hz and were 1.33 deg visual angle in diameter. Each grating was displayed in the center of the right or left half of the screen. The specific task and condition determined which side of the screen each grating was drawn on. When viewed through the stereoscope, the two gratings were superimposed, one on top of the other. Surrounding each grating was a square checkerboard pattern (0.17 deg width, 1.53 deg length) to promote the fusion of the two eyes in the rest of the visual field.

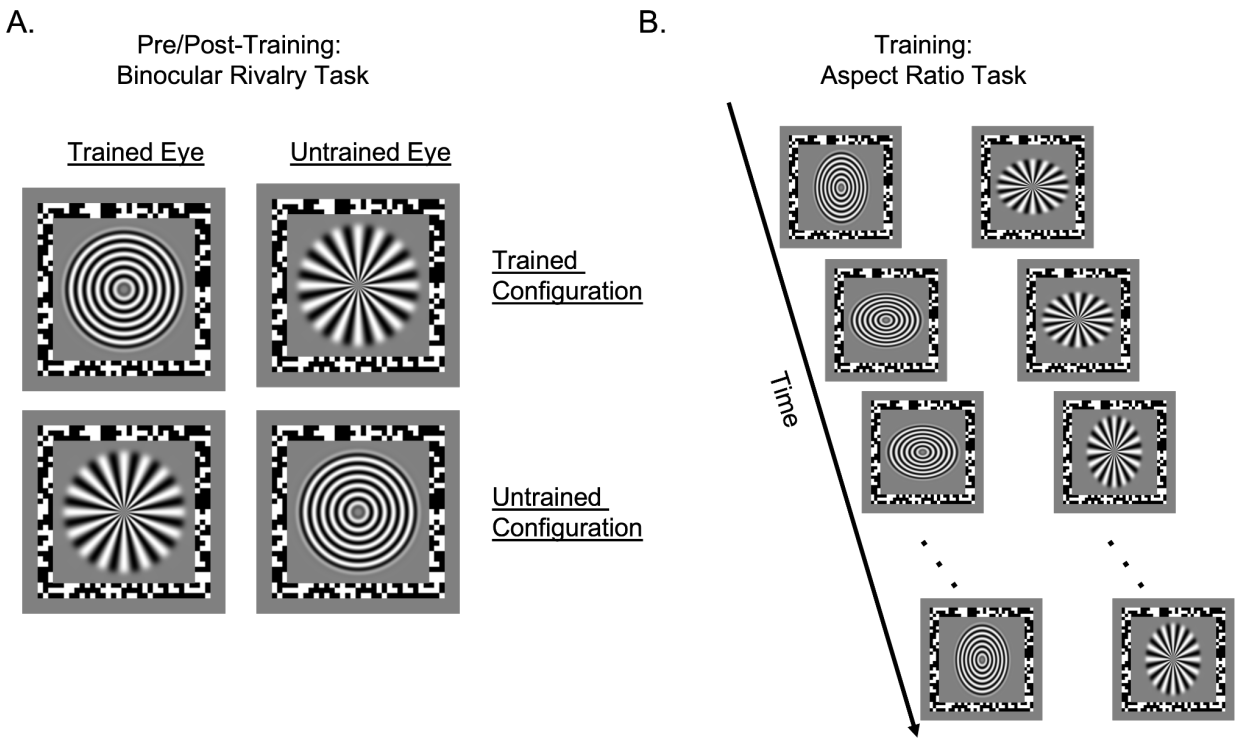

Figure 14. Visual stimuli and time course for each task. A) During the binocular rivalry task, participants passively viewed the stimuli and reported which grating was perceived or a mixed percept. The first eight blocks followed the trained configuration, and the last four blocks followed an untrained configuration. B) During the aspect ratio task, both gratings changed shape from tall to wide and vice versa at different rates. The bull's eye grating shape change occurred at a 0.7 probability at 0.7 Hz, and the stripes grating shape change occurred at a 0.5 probability at 0.7 Hz. The participant was asked to report the shape change of the bull's eye or when the stripes or mix were perceived.

2.3 Experiment Timeline

Each participant completed two tasks: rivalry and aspect ratio. In rivalry, observers reported which eye they perceived or a mixture. In the aspect ratio task, participants reported whether the bulls-eye was tall or wide or if they perceived stripes or a mixture. There were four kinds of sessions: eye dominance, rivalry pre-test, training, and rivalry post-test. The rivalry task was presented during eye dominance and rivalry sessions, and the aspect ratio task was presented during training sessions. On day 1, the participant completed the eye dominance session and the rivalry pre-test session. On days 2-13, the

participant completed training sessions. On day 13, the participant completed a rivalry post-test session immediately after the last training session. Participants were encouraged to complete all sessions on consecutive days and were allowed to take up to two consecutive days off twice during the entirety of the experiment.

2.4 Eye dominance session

A binocular rivalry task was used to measure eye dominance for the purposes of determining the weaker eye to train. The bull's eye and radial gratings were presented without any aspect ratio changes, and the participant was asked to report when they perceived each grating or when they perceived a mixture of the two. The task consisted of 10 blocks that each lasted 60 sec. Which grating was presented to each eye changed every block to control for any influence the specific grating might have on perception. The results from this task were used to determine the participant's natural sensory eye dominance by measuring the amount of time the participant spent seeing one grating compared to the other. The eye that averaged the least perceptual time in the initial session was chosen for training. If neither eye was dominant on the first day, the left/right eye was randomly selected for training.

2.5 Pre/post-training sessions

Before and after training, a binocular rivalry task was used to track any changes to perceptual dominance and temporal dynamics. This task was similar to the task used during the eye dominance session, except that the stimulus configuration remained unchanged. The task consisted of 12 blocks that each lasted 120 sec. In eight blocks, the bull's eye grating was presented to the dominant eye (trained configuration), and in four

blocks, the gratings were switched across the eyes (untrained configuration) (Figure 14A). The participant was asked to report anytime they perceived a change in which grating was dominant or if they perceived a mix of the two gratings.

2.6 Training sessions

We used a modified version of the aspect ratio task described by Dieter et al., 2016. In this task, the bull's eye grating was presented to the trained eye (chosen on day 1). We manipulated the aspect ratio of both gratings, changing it to either look like a vertical or horizontal oval (Figure 14B). Both gratings changed shape from tall to wide and vice versa at different rates. The bull's eye grating shape change occurred at a 0.7 probability at 0.7 Hz, and the shape change of the stripes grating occurred at a 0.5 probability at 0.7 Hz. The participant was asked to report any time their perception changes and to track the shape change of the bull's eye grating, such as tall/wide bull's eye grating, stripes, or mix. The size of the aspect ratio change of the bull's eye grating was determined by a two-down, one-up staircase with 8 step changes. Two consecutive correct answers resulted in the change becoming smaller and, therefore, harder to detect. The staircase checked for a correct shape judgment every 1.4 s. During each session, participants completed 14 blocks that lasted 2 min each, except for one participant who completed eight blocks on the last day due to reported eye strain.

3. Results

3.1 Pre/post-training rivalry task

Trained Configuration Percept durations for the trained and untrained eye followed a gamma distribution in the binocular rivalry task for most subjects (Figure 15),

consistent with past work (Blake et al., 1971). Percept durations were generally longer in the pre-training rivalry session than in the post-training session for all three states (Figure 16B). The experiment timeline could have caused this since the post-training rivalry task occurred on the last day immediately after 28 minutes of the aspect ratio task. Extended periods of time spent experiencing binocular rivalry can cause faster switches between states and more mixtures (Klink et al., 2010; Suzuki & Grabowecky, 2007). Overall percept durations were shorter than in the work on which this study was based (Dieter et al., 2016), likely due to the stimuli being presented at full contrast, compared to 25% in the previous study, which can cause shorter durations in any given state (Levelt, 1965).

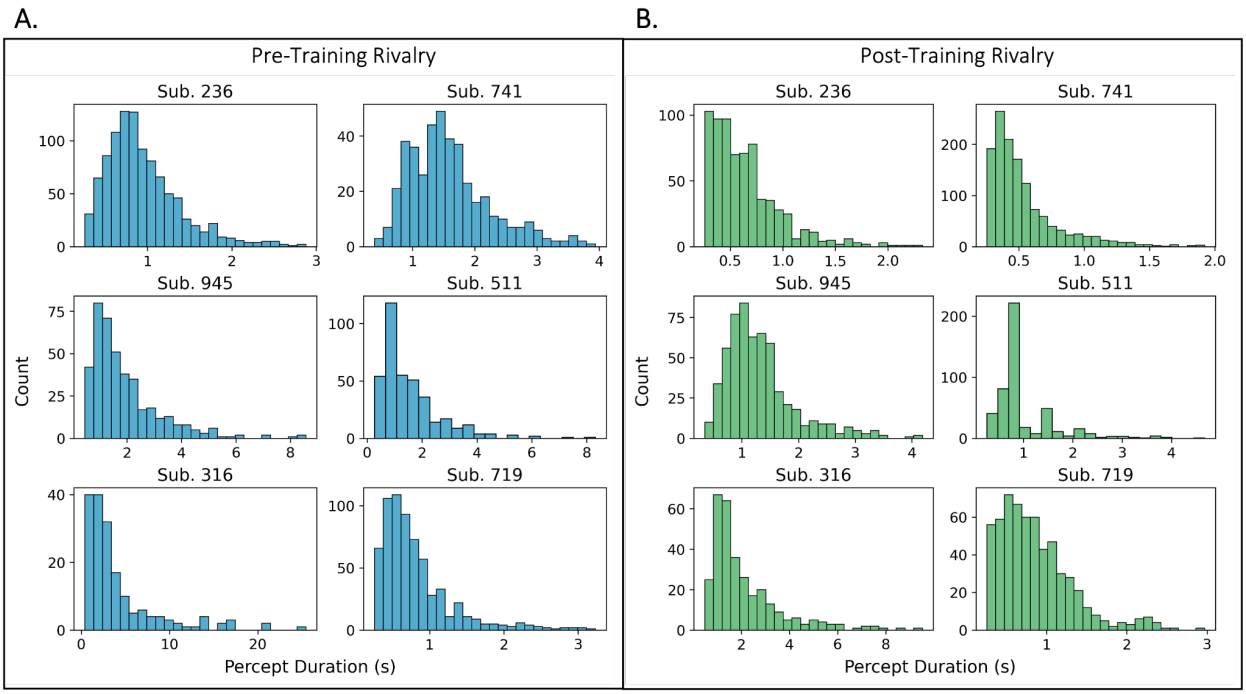

Figure 15. Percept durations distributions for each participant and rivalry session for trained and untrained eyes combined. A) pre-training rivalry session, B) post-training rivalry session.

In the pre-training rivalry session, most participants had higher mean percept durations for the untrained eye than the trained eye or equal durations across states (Figure 16A). This makes sense because the trained eye was selected as the weaker eye based on the eye dominance task.

Following training, percept durations were generally equal or slightly longer for the trained eye than the untrained eye (Figure 16B). A two-way ANOVA was conducted that examined the effect of the session and perceptual state on percept duration. There was no statistically significant interaction between the effects of the session and state on percept duration, $F(2, 30) = 1.20$ $p = 0.31$). However, there was a significant main effect of the session on the percept duration ($p<0.05$); therefore, we conducted two post hoc comparisons to understand this effect. Percept durations in the pre-training rivalry were shorter for the trained eye ($M=1.30$, $SD = 0.43$) than the untrained eye ($M=1.95$, $SD = 1.28$), but this difference was not significant ($t(5) = -1.43$, $p =0.21$). This trend reversed in the post-training session, where the trained eye's percept durations ($M=1.15$, $SD = 0.71$) were longer than the untrained eye ($M=0.90$, $SD = 0.35$); however, this difference was also not significant ($t(5) = 1.18$, $p=0.29$).

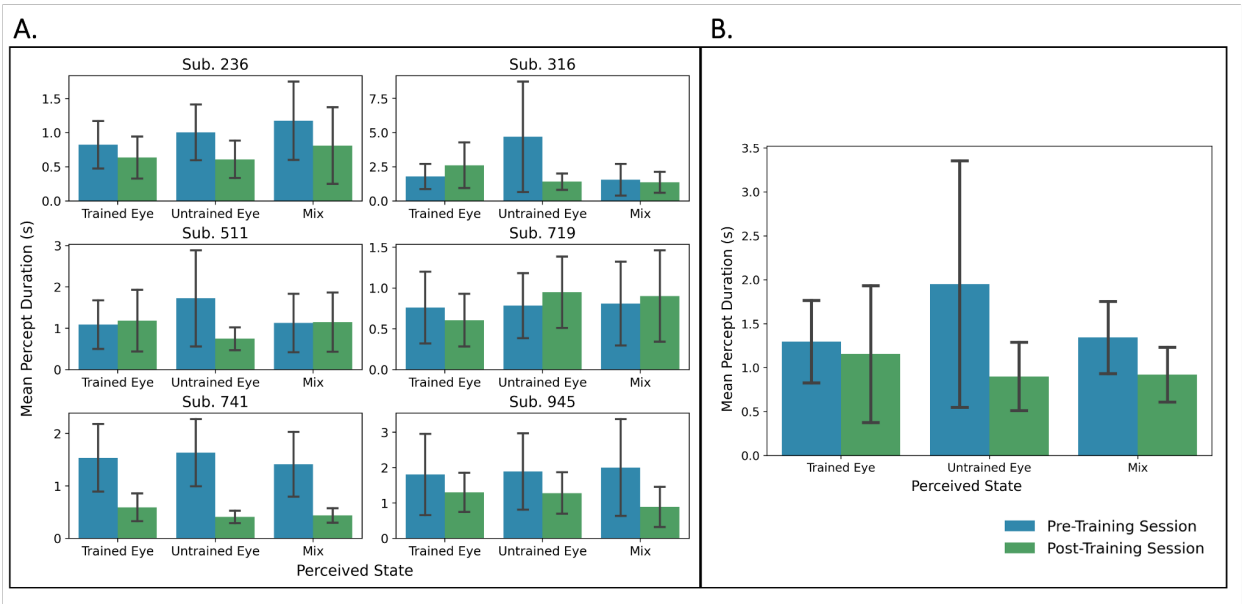

Figure 16. Mean percept durations for each rivalry session and each state. A) Across participants. B) For all participants combined. In both figures, the blue bar is the pre-training rivalry, and the green bar is the post-training rivalry. Error bars represent the standard deviation in each state.

We also quantified the total duration spent in each state within the 2-minute blocks in each session. In the pre-training session, most participants had a higher mean total duration for the untrained eye than for the trained eye (Figure 17A). However, in the post-training session, the total duration was generally higher for the trained eye than the untrained eye (Figure 17). A two-way ANOVA was conducted that examined the effect of the session and perceptual state on total duration in rivalry. There was a statistically significant interaction between the effects of the session and state on duration, $F(2, 30) = 4.44$, $p < .05$. Three post-hoc contrasts were conducted to unpack this effect. Total block durations in the pre-training rivalry were shorter for the trained eye ($M=31.20$, $SD = 14.38$) than the untrained eye ($M=52.14$, $SD = 11.97$) ($t(5)= -2.25$, $p < .05$). This trend reversed in the post-training session, where the trained eye's total durations ($M=39.12$, $SD = 16.14$) were longer than the untrained eye ($M=31.12$, $SD = 11.43$); however, this

difference was not significant (t(5) = 0.76, p=0.76). The change in the difference between eyes from pre- to post-training rivalry showed a trend that approached significance (t(5) = -1.78, p =0.07).

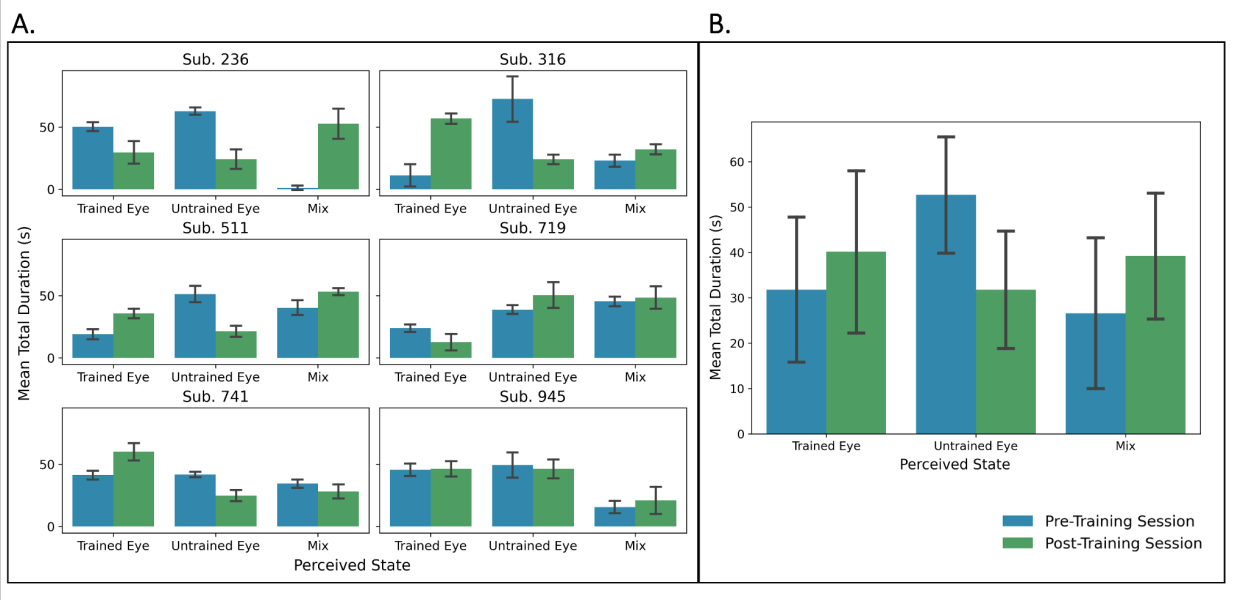

Figure 17. Mean total durations for each rivalry session and each state across blocks. A) Across participants, B) For all participants combined. In both figures, the blue bar is the pre-training rivalry, and the green bar is the post-training rivalry. Error bars represent the standard deviation in each state.

Untrained Configuration For the last four blocks of both pre- and post-training sessions, the stimulus configuration was switched so that the trained stimulus (bull's eye grating) was presented to the untrained eye. Like the trained configuration, percept durations were generally longer in the pre-training session than in the post-training session for all three states in the untrained configuration. In both sessions, most participants had roughly equal mean percept durations for the two eyes (Figure 18A). A two-way ANOVA was conducted that examined the effect of the session and perceptual

state on percept duration in rivalry. There was no significant interaction between the effects of the session and state on percept duration (F (2, 30) = 0.09, p = 0.91).

We also examined the total duration spent in each state in each block for the untrained configuration. In the pre-training rivalry session, the mean total duration for the trained eye was roughly equal to the untrained eye. However, in the post-training session, the mean of the trained eye was higher than the untrained eye (Figure 18B). A two-way ANOVA was conducted that examined the effect of the session and perceptual state on total block duration in rivalry. Again, there was no significant interaction between the effects of the session and state on duration (F (2, 30) = 0.75, p=0.48).

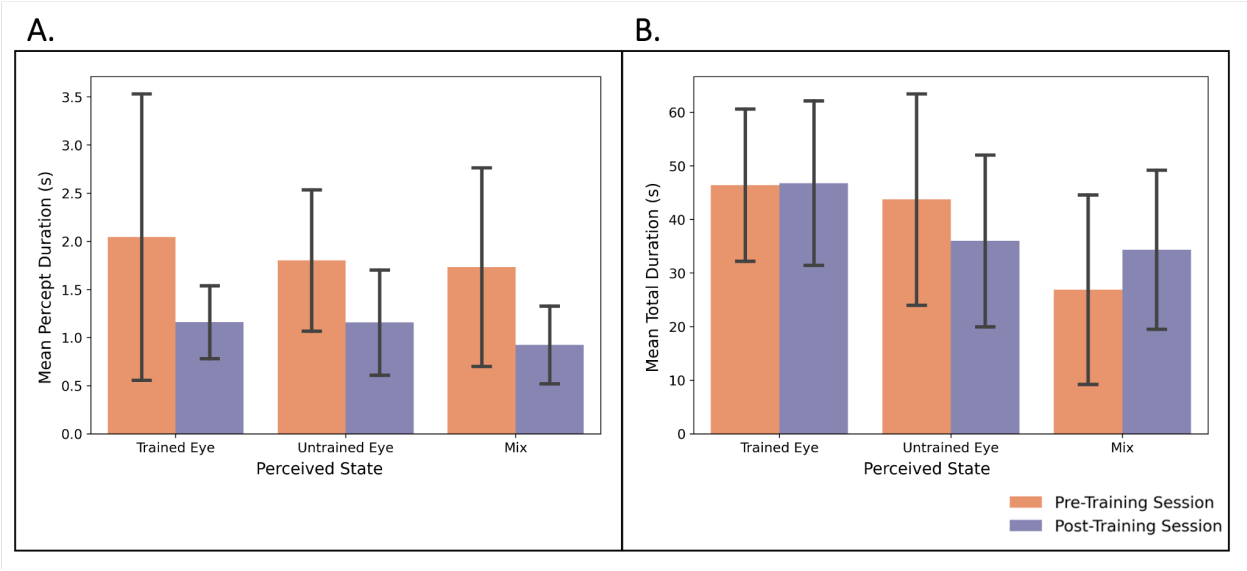

Figure 18. Mean durations for the untrained configuration. The trained (bull's eye) grating was presented to the untrained eye. A) Mean rivalry percept durations across sessions. B) Mean rivalry total block durations across sessions.

3.2 Aspect ratio task

In the aspect ratio task, for most participants, mean percept durations trended downward across sessions, meaning that percept durations became shorter as more

training sessions were completed (Figure 19A). Percept durations generally had a steeper negative trend for the untrained eye than for the trained eye (Figure 19B). A series of t-tests were conducted to compare the differences in slope between the trained eye durations and the untrained eye durations across sessions and across participants. Percept durations in the trained eye had a negative slope (M=-0.03, SD=0.06), but this was not significant (t(5) = -1.26, p =0.13). The untrained eye also had a negative slope (M=-0.03, SD=0.04) which approached significance (t(5)= -1.88, p = 0.06). The difference between the two slopes was also not significant (t(5) =-0.06, p =0.95).

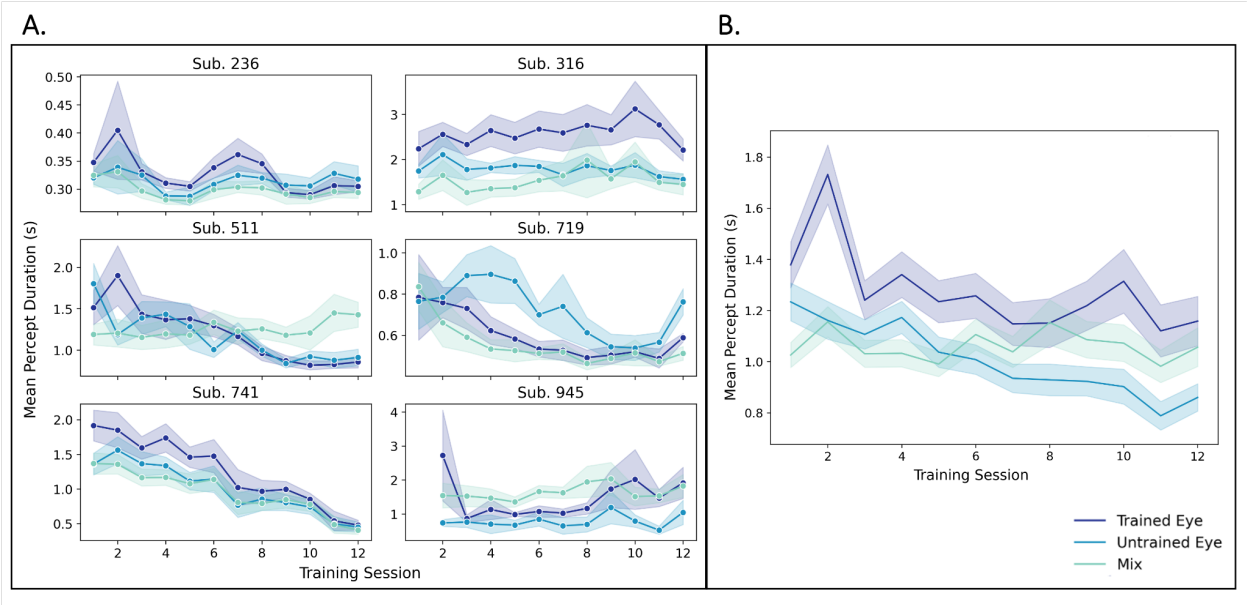

Figure 19. Mean percept durations in the aspect ratio task across training sessions. Results for both figures are in seconds, and the shaded area is the standard error. A) Results for each participant. B) Results collapsed across participants

In the aspect ratio task, for most participants, the total duration for a given percept tended to stay constant for the trained eye, trended negative for the untrained eye, and trended positive for mixed percepts (Figure 20A). This means that for the total duration as more sessions were completed, participants spent more time perceiving a mixture,

roughly the same amount of time perceiving the trained eye, and less time perceiving the untrained eye (Figure 20B). t-tests were conducted to compare the differences in slope between the trained eye and the untrained eye across sessions. Total duration in the trained eye had a positive slope (M=0.21, SD=0.61), but this trend was not significant (t(5) = 0.77, p =0.75). Total duration in the untrained eye had a negative slope (M=-0.94, SD=1.13) which was close to, but not significant (t(5) =-1.86, p =0.06). However, the difference between the two slopes was significant (t(5) =2.79, p <0.05).

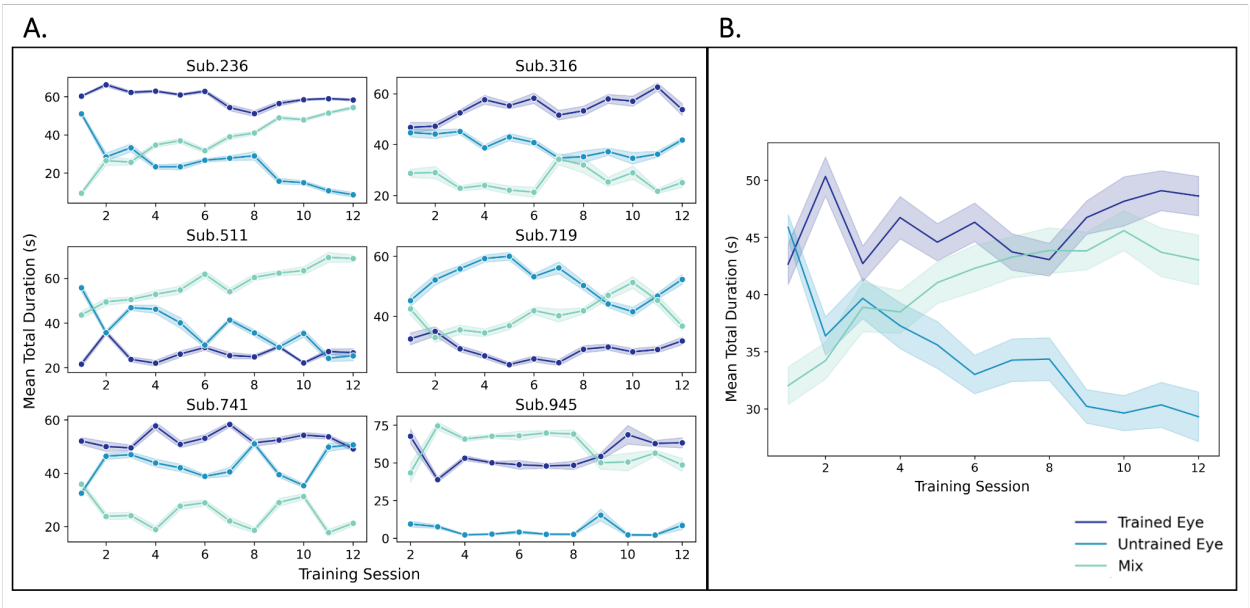

Figure 20. Mean total block durations in the aspect ratio task across training sessions. Results for both figures are in seconds, and the shaded area is the standard error. A) Results for each participant. B) Results collapsed across participants

4. Discussion

Some of our results validate what was found by Dieter et al., (2016); through perceptual training, temporal dynamics in binocular rivalry can be manipulated, especially in our case, the total duration observers perceived the stimulus in the trained eye vs. the untrained eye. We found that the total duration shifted towards the trained eye pre-

training to post-training. This indicates that training influenced eye dominance dynamics during binocular rivalry. However, the effect reported by Dieter et al., 2016 was much stronger than our effects, and they reported from 80% dominance to exclusive dominance of the trained eye in post-training rivalry.

We failed to find such a significant effect, likely due to the differences in experimental design. One major difference was that we presented our visual stimuli at full contrast (compared to 25% contrast in their study), which can cause faster durations and could therefore impact how long the participants perceived each state. We also opted for a two-down, one-up staircase with 8-step changes in the diameter of the trained grating compared to the previous study, which adjusted the diameter of the grating adaptively between sessions to ensure difficulty in the task.

During piloting, we found that asking the participants to attend to changes in the aspect ratio of one grating greatly increased the total duration for that grating. Therefore, we modified our experiment design further so there would be no bias between the two gratings. The previous study only manipulated the shape of one grating. However, we had an aspect ratio change occur in both stimuli, at different times, so the change in the shape of one grating could not cause a switch in the perceptual state.

We also changed how responses were collected. The previous study used a two-alternative, forced-choice method to collect responses, where the participant reported tall or wide continuously and simply guessed while seeing the other stimulus. In our experiment, participants were asked to report tall, wide, or the other grating. We also thought it was necessary to ask participants to respond when a mixture was seen to understand if the initial imbalance in training was due to the participant performing the

shape change task while in a mixed state. The total duration for the mixed state consistently increased within and between sessions in our final experiment; this result aligns with previous studies that found an increase in mixture with prolonged exposure to rivalry (Klink et al., 2010). It is possible that the results found by Dieter et al., 2016 are partially attributed to an overrepresentation of the mixed state.

Two other studies have investigated if perceptual learning can influence binocular rivalry. Their reported effects are more aligned with our results, where improvement in the task-relevant stimulus is significant but does not result in an exclusive perception of the trained stimulus (Paffen et al., 2008; Xu et al., 2010).

Our analyses considered both percept duration and total duration. Percept duration measures the duration of each time a state is perceived, while total duration encapsulates the proportion of time each state dominated over the entire session. Both measures were important because the switch rate could be affected by training differently than the total duration. For example, Dieter et al., 2016 reported a single percept being stable for tens of seconds before a switch was reported. However, we found the opposite effect where the switch rate increased post-training, meaning that the percept durations were shorter. Although our percept durations were shorter, we also saw an increase in total duration for the trained eye post-training. This means that although percepts switched faster between states overall, the participants saw the trained stimuli more often within the session.

Results varied between participants; four of our six participants demonstrated a trend for learning where the trained eye became more dominant post-training. One participant showed equal durations across sessions, and one participant (Sub. 719)

showed a reversed trend (Figure 17A). It is unclear why the trend reversed for this participant. The aspect ratio task data reveal that the participant was clearly trying during each session, as they reached the smallest aspect ratio changes before the staircase reset. Across sessions, they reach the smallest change faster, which indicates learning. However, from their total durations across sessions, it is clear that they spent more time perceiving stimuli in the untrained eye. It is possible that more training sessions could have been beneficial to see a clear learning effect in this participant. Dieter et al., 2016 reported extending training sessions for one participant from 12 to 24 sessions who had a large eye imbalance.

It is also possible that the demanding aspect of the experiment could have influenced the performance of this participant. On the last day, this participant mentioned experiencing exhaustion and eye strain toward the end of the final training session. The participant was asked if they wanted to end the session, but they opted for a shortened training session followed by a break and then completion of the post-training rivalry task. This could have influenced post-training rivalry results.

In other analyses, we switched the stimulus configuration where the trained grating (bull's eye) was presented to the untrained eye to see if learning would follow the stimulus and transfer to the untrained eye. The changes found in total durations were insignificant; therefore, we cannot conclude that this effect is either eye-specific or stimulus-specific.

Lastly, we had planned to follow up on these results using high-resolution (7T) fMRI and scan participants before and after undergoing this kind of perceptual learning paradigm. Using high-resolution fMRI would have allowed us to quantify eye selectivity across cortical depth of V1. Laminar profiles from before and after training would have

allowed us to understand how perceptual learning affects neural activation for eye selectivity at submillimeter levels in V1. However, the effects caused by perceptual learning were not large enough to justify pursuing this kind of study.

References

Adams, D. L., Sincich, L. C., & Horton, J. C. (2007). Complete Pattern of Ocular Dominance Columns in Human Primary Visual Cortex. *Journal of Neuroscience*, *27*(39), 10391–10403. https://doi.org/10.1523/JNEUROSCI.2923-07.2007

Adriany, G., Waks, M., Tramm, B., Schillak, S., Yacoub, E., de Martino, F., de Moortele, P.-F. V., Naselaris, T., Vaughan, T., & Ugurbil, K. (2012). *An Open Faced 4 ch. Loop Transmit / 16 ch. Receive Array Coil for HiRes fMRI at 7 Tesla*. ISMRM. https://archive.ismrm.org/2012/0429.html

An, X., Gong, H., Qian, L., Wang, X., Pan, Y., Zhang, X., Yang, Y., & Wang, W. (2012). Distinct Functional Organizations for Processing Different Motion Signals in V1, V2, and V4 of Macaque. *Journal of Neuroscience*, *32*(39), 13363–13379. https://doi.org/10.1523/JNEUROSCI.1900-12.2012

Anderson, S. J., Mullen, K. T., & Hess, R. F. (1991). Human peripheral spatial resolution for achromatic and chromatic stimuli: Limits imposed by optical and retinal factors. *The Journal of Physiology*, *442*(1), 47–64. https://doi.org/10.1113/jphysiol.1991.sp018781

Başgöze, Z., Mackey, A. P., & Cooper, E. A. (2018). Plasticity and Adaptation in Adult Binocular Vision. *Current Biology*, *28*(24), R1406–R1413. https://doi.org/10.1016/j.cub.2018.10.024

Benson, N. C., Butt, O. H., Brainard, D. H., & Aguirre, G. K. (2014). Correction of Distortion in Flattened Representations of the Cortical Surface Allows Prediction of V1-V3 Functional Organization from Anatomy. *PLOS Computational Biology*, *10*(3), e1003538. https://doi.org/10.1371/journal.pcbi.1003538

Bilodeau, L., & Faubert, J. (1997). Isoluminance and chromatic motion perception throughout the visual field. *Vision Research*, *37*(15), 2073–2081. https://doi.org/10.1016/S0042-6989(97)00012-6

Blake, Fox, R., & McIntyre, C. (1971). Stochastic properties of stabilized-image binocular rivalry alternations. *Journal of Experimental Psychology*, *88*(3), 327. https://doi.org/10.1037/h0030877

Blake, R., & Logothetis, N. K. (2002). Visual competition. *Nature Reviews Neuroscience*, *3*(1), Article 1. https://doi.org/10.1038/nrn701

Blake, R., Zimba, L., & Williams, D. (1985). Visual motion, binocular correspondence and binocular rivalry. *Biological Cybernetics*, *52*(6), 391–397. https://doi.org/10.1007/BF00449596

Blasdel, G. G., & Lund, J. S. (1983). Termination of afferent axons in macaque striate cortex. *Journal of Neuroscience*, *3*(7), 1389–1413. https://doi.org/10.1523/JNEUROSCI.03-07-01389.1983

Blasdel, G. G., & Salama, G. (1986). Voltage-sensitive dyes reveal a modular organization in monkey striate cortex. *Nature*, *321*(6070), Article 6070. https://doi.org/10.1038/321579a0

Bonhoeffer, T., & Grinvald, A. (1991). Iso-orientation domains in cat visual cortex are arranged in pinwheel-like patterns. *Nature*, *353*(6343), Article 6343. https://doi.org/10.1038/353429a0

Braitenberg, V., & Braitenberg, C. (1979). Geometry of orientation columns in the visual cortex. *Biological Cybernetics*, *33*(3), 179–186. https://doi.org/10.1007/BF00337296

Brascamp, J. W., Klink, P. C., & Levelt, W. J. M. (2015). The ‘laws’ of binocular rivalry: 50 years of Levelt’s propositions. *Vision Research*, *109*, 20–37. https://doi.org/10.1016/j.visres.2015.02.019

Burkhalter, A., & Bernardo, K. L. (1989). Organization of corticocortical connections in human visual cortex. *Proceedings of the National Academy of Sciences*, *86*(3), 1071–1075. https://doi.org/10.1073/pnas.86.3.1071

Calkins, D. J., Schein, S. J., Tsukamoto, Y., & Sterling, P. (1994). M and L cones in macaque fovea connect to midget ganglion cells by different numbers of excitatory synapses. *Nature*, *371*(6492), Article 6492. https://doi.org/10.1038/371070a0

Callaway, E. M. (2005). Structure and function of parallel pathways in the primate early visual system. *The Journal of Physiology*, *566*(1), 13–19. https://doi.org/10.1113/jphysiol.2005.088047

Callaway, E. M., & Wiser, A. K. (1996). Contributions of individual layer 2–5 spiny neurons to local circuits in macaque primary visual cortex. *Visual Neuroscience*, *13*(5), 907–922. https://doi.org/10.1017/S0952523800009159

Carey, D. P. (2001). Vision research: Losing sight of eye dominance. *Current Biology*, *11*(20), R828–R830. https://doi.org/10.1016/S0960-9822(01)00496-1

Chatterjee, S., & Callaway, E. M. (2003). Parallel colour-opponent pathways to primary visual cortex. *Nature*, *426*(6967), Article 6967. https://doi.org/10.1038/nature02167

Chen, G., Dan, Y., & Li, C.-Y. (2005). Stimulation of non-classical receptive field enhances orientation selectivity in the cat. *The Journal of Physiology*, *564*(Pt 1),

233–243. https://doi.org/10.1113/jphysiol.2004.080051

Chen, G., Lu, H. D., & Roe, A. W. (2008). A Map for Horizontal Disparity in Monkey V2. *Neuron*, *58*(3), 442–450. https://doi.org/10.1016/j.neuron.2008.02.032

Cho, S., Roy, A., Liu, C. J., Idiyatullin, D., Zhu, W., Zhang, Y., Zhu, X.-H., O'Herron, P., Leikvoll, A., Chen, W., Kara, P., & Uğurbil, K. (2022). Cortical layer-specific differences in stimulus selectivity revealed with high-field fMRI and single-vessel resolution optical imaging of the primary visual cortex. *NeuroImage*, *251*, 118978. https://doi.org/10.1016/j.neuroimage.2022.118978

Chong, S. C., Tadin, D., & Blake, R. (2005). Endogenous attention prolongs dominance durations in binocular rivalry. *Journal of Vision*, *5*(11), 1004–1012. https://doi.org/10.1167/5.11.6

Cohen, J. (1952). Eye-Dominance. *The American Journal of Psychology*, *65*(4), 634–636. https://doi.org/10.2307/1418050

Dacey, D. M., & Lee, B. B. (1994). The "blue-on" opponent pathway in primate retina originates from a distinct bistratified ganglion cell type. *Nature*, *367*(6465), Article 6465. https://doi.org/10.1038/367731a0

Denison, R. N., Vu, A. T., Yacoub, E., Feinberg, D. A., & Silver, M. A. (2014). Functional mapping of the magnocellular and parvocellular subdivisions of human LGN. *NeuroImage*, *102*, 358–369. https://doi.org/10.1016/j.neuroimage.2014.07.019

Derrington, A. M., & Lennie, P. (1984). Spatial and temporal contrast sensitivities of neurones in lateral geniculate nucleus of macaque. *The Journal of Physiology*, *357*(1), 219–240. https://doi.org/10.1113/jphysiol.1984.sp015498

Desimone, R., Schein, S. J., Moran, J., & Ungerleider, L. G. (1985). Contour, color and

shape analysis beyond the striate cortex. *Vision Research*, *25*(3), 441–452. https://doi.org/10.1016/0042-6989(85)90069-0

Dieter, K. C., Melnick, M. D., & Tadin, D. (2016). Perceptual training profoundly alters binocular rivalry through both sensory and attentional enhancements. *Proceedings of the National Academy of Sciences*, *113*(45), 12874–12879. https://doi.org/10.1073/pnas.1602722113

Dieter, K. C., Sy, J. L., & Blake, R. (2017). Individual differences in sensory eye dominance reflected in the dynamics of binocular rivalry. *Vision Research*, *141*, 40–50. https://doi.org/10.1016/j.visres.2016.09.014

Ding, Y., Naber, M., Gayet, S., Stigchel, S. V. der, & Paffen, C. L. E. (2018). Assessing the generalizability of eye dominance across binocular rivalry, onset rivalry, and continuous flash suppression. *Journal of Vision*, *18*(6), 6–6. https://doi.org/10.1167/18.6.6

Dumoulin, S. O., Harvey, B. M., Fracasso, A., Zuiderbaan, W., Luijten, P. R., Wandell, B. A., & Petridou, N. (2017). In vivo evidence of functional and anatomical stripe-based subdivisions in human V2 and V3. *Scientific Reports*, *7*(1), Article 1. https://doi.org/10.1038/s41598-017-00634-6

Dumoulin, S. O., & Wandell, B. A. (2008). Population receptive field estimates in human visual cortex. *NeuroImage*, *39*(2), 647–660. https://doi.org/10.1016/j.neuroimage.2007.09.034

Engel, S. A., Glover, G. H., & Wandell, B. A. (1997). Retinotopic organization in human visual cortex and the spatial precision of functional MRI. *Cerebral Cortex*, *7*(2), 181–192. https://doi.org/10.1093/cercor/7.2.181

Fang, C., Cai, X., & Lu, H. D. (2022). Orientation anisotropies in macaque visual areas. *Proceedings of the National Academy of Sciences*, *119*(15), e2113407119. https://doi.org/10.1073/pnas.2113407119

Fracasso, A., van Veluw, S. J., Visser, F., Luijten, P. R., Spliet, W., Zwanenburg, J. J. M., Dumoulin, S. O., & Petridou, N. (2016). Lines of Baillarger in vivo and ex vivo: Myelin contrast across lamina at 7T MRI and histology. *NeuroImage*, *133*, 163–175. https://doi.org/10.1016/j.neuroimage.2016.02.072

Freeman, J., Brouwer, G. J., Heeger, D. J., & Merriam, E. P. (2011). Orientation Decoding Depends on Maps, Not Columns. *Journal of Neuroscience*, *31*(13), 4792–4804. https://doi.org/10.1523/JNEUROSCI.5160-10.2011

Freeman, J., Heeger, D. J., & Merriam, E. P. (2013). Coarse-Scale Biases for Spirals and Orientation in Human Visual Cortex. *Journal of Neuroscience*, *33*(50), 19695–19703. https://doi.org/10.1523/JNEUROSCI.0889-13.2013

Furmanski, C. S., & Engel, S. A. (2000). An oblique effect in human primary visual cortex. *Nature Neuroscience*, *3*(6), Article 6. https://doi.org/10.1038/75702

Griswold, M. A., Jakob, P. M., Heidemann, R. M., Nittka, M., Jellus, V., Wang, J., Kiefer, B., & Haase, A. (2002). Generalized autocalibrating partially parallel acquisitions (GRAPPA). *Magnetic Resonance in Medicine*, *47*(6), 1202–1210. https://doi.org/10.1002/mrm.10171

Havlicek, M., & Uludağ, K. (2020). A dynamical model of the laminar BOLD response. *NeuroImage*, *204*, 116209. https://doi.org/10.1016/j.neuroimage.2019.116209

Hockfield, S., Tootell, R. B., & Zaremba, S. (1990). Molecular differences among neurons reveal an organization of human visual cortex. *Proceedings of the*

National Academy of Sciences, *87*(8), 3027–3031. https://doi.org/10.1073/pnas.87.8.3027

Horiguchi, H., Nakadomari, S., Misaki, M., & Wandell, B. A. (2009). Two temporal channels in human V1 identified using fMRI. *NeuroImage*, *47*(1), 273–280. https://doi.org/10.1016/j.neuroimage.2009.03.078

Horton, J. C. (1984). Cytochrome oxidase patches: A new cytoarchitectonic feature of monkey visual cortex. *Philosophical Transactions of the Royal Society of London. B, Biological Sciences*, *304*(1119), 199–253. https://doi.org/10.1098/rstb.1984.0021

Hubel, D. H., & Livingstone, M. S. (1985). Complex–unoriented cells in a subregion of primate area 18. *Nature*, *315*(6017), Article 6017. https://doi.org/10.1038/315325a0

Hubel, D. H., & Livingstone, M. S. (1990). Color and contrast sensitivity in the lateral geniculate body and primary visual cortex of the macaque monkey. *Journal of Neuroscience*, *10*(7), 2223–2237. https://doi.org/10.1523/JNEUROSCI.10-07-02223.1990

Hubel, D. H., & Wiesel, T. N. (1959). Receptive fields of single neurones in the cat's striate cortex. *The Journal of Physiology*, *148*(3), 574–591. https://doi.org/10.1113/jphysiol.1959.sp006308

Hubel, D. H., & Wiesel, T. N. (1962). Receptive fields, binocular interaction and functional architecture in the cat's visual cortex. *The Journal of Physiology*, *160*(1), 106–154. https://doi.org/10.1113/jphysiol.1962.sp006837

Hubel, D. H., Wiesel, T. N., & Stryker, M. P. (1978). Anatomical demonstration of

orientation columns in macaque monkey. *Journal of Comparative Neurology*, *177*(3), 361–379. https://doi.org/10.1002/cne.901770302

Huber, L., Handwerker, D. A., Jangraw, D. C., Chen, G., Hall, A., Stüber, C., Gonzalez-Castillo, J., Ivanov, D., Marrett, S., Guidi, M., Goense, J., Poser, B. A., & Bandettini, P. A. (2017). High-Resolution CBV-fMRI Allows Mapping of Laminar Activity and Connectivity of Cortical Input and Output in Human M1. *Neuron*, *96*(6), 1253-1263.e7. https://doi.org/10.1016/j.neuron.2017.11.005

Kandel, E. R., Schwartz, J. H., Essell, T. M., Siegelbaum, S., & Hudspeth, A. J. (2000). *Principles of Neural Science, Fifth Edition | AccessBiomedical Science | McGraw Hill Medical* (Vol. 1–4). McGraw-hill. https://accessbiomedicalscience.mhmedical.com/content.aspx?bookid=1049&sectionid=59138139

Kaplan, E., & Shapley, R. M. (1982). X and Y cells in the lateral geniculate nucleus of macaque monkeys. *The Journal of Physiology*, *330*(1), 125–143. https://doi.org/10.1113/jphysiol.1982.sp014333

Kaschube, M., Schnabel, M., Löwel, S., Coppola, D. M., White, L. E., & Wolf, F. (2010). Universality in the Evolution of Orientation Columns in the Visual Cortex. *Science*, *330*(6007), 1113–1116. https://doi.org/10.1126/science.1194869

Kashyap, S., Ivanov, D., Havlicek, M., Poser, B. A., & Uludağ, K. (2018). Impact of acquisition and analysis strategies on cortical depth-dependent fMRI. *NeuroImage*, *168*, 332–344. https://doi.org/10.1016/j.neuroimage.2017.05.022

Keller, A. L., Schüz, A., Logothetis, N. K., & Weber, B. (2011). Vascularization of Cytochrome Oxidase-Rich Blobs in the Primary Visual Cortex of Squirrel and

Macaque Monkeys. *Journal of Neuroscience*, *31*(4), 1246–1253. https://doi.org/10.1523/JNEUROSCI.2765-10.2011

Klink, P. C., Brascamp, J. W., Blake, R., & van Wezel, R. J. A. (2010). Experience-Driven Plasticity in Binocular Vision. *Current Biology*, *20*(16), 1464–1469. https://doi.org/10.1016/j.cub.2010.06.057

Kok, P., Bains, L. J., van Mourik, T., Norris, D. G., & de Lange, F. P. (2016). Selective Activation of the Deep Layers of the Human Primary Visual Cortex by Top-Down Feedback. *Current Biology*, *26*(3), 371–376. https://doi.org/10.1016/j.cub.2015.12.038

Landler, L., Ruxton, G. D., & Malkemper, E. P. (2021). Advice on comparing two independent samples of circular data in biology. *Scientific Reports*, *11*(1), Article 1. https://doi.org/10.1038/s41598-021-99299-5

Larsson, J., Harrison, C., Jackson, J., Oh, S.-M., & Zeringyte, V. (2017). Spatial scale and distribution of neurovascular signals underlying decoding of orientation and eye of origin from fMRI data. *Journal of Neurophysiology*, *117*(2), 818–835. https://doi.org/10.1152/jn.00590.2016

Levelt, W. J. (1965). On binocular rivalry. *Doctoral Dissertation, Van Gorcum Assesn*. https://pure.mpg.de/rest/items/item_77195/component/file_2424565/content

Li, X., Zhu, Q., Janssens, T., Arsenault, J. T., & Vanduffel, W. (2019). In Vivo Identification of Thick, Thin, and Pale Stripes of Macaque Area V2 Using Submillimeter Resolution (f)MRI at 3 T. *Cerebral Cortex*, *29*(2), 544–560. https://doi.org/10.1093/cercor/bhx337

Livingstone, M., & Hubel, D. (1988). Segregation of Form, Color, Movement, and Depth:

Anatomy, Physiology, and Perception. *Science*, *240*(4853), 740–749. https://doi.org/10.1126/science.3283936

Livingstone, M. S., & Hubel, D. H. (1988). Do the relative mapping densities of the magno- and parvocellular systems vary with eccentricity? *Journal of Neuroscience*, *8*(11), 4334–4339. https://doi.org/10.1523/JNEUROSCI.08-11-04334.1988

Lu, H. D., & Roe, A. W. (2007). Optical Imaging of Contrast Response in Macaque Monkey V1 and V2. *Cerebral Cortex*, *17*(11), 2675–2695. https://doi.org/10.1093/cercor/bhl177

Lyu, L., Han, Q., He, X., & Bao, M. (2020). *Eye-specific voluntary attention can induce a shift of perceptual ocular dominance* (p. 2020.08.03.233759). https://doi.org/10.1101/2020.08.03.233759

Mannion, D. J., McDonald, J. S., & Clifford, C. W. G. (2010). Orientation Anisotropies in Human Visual Cortex. *Journal of Neurophysiology*, *103*(6), 3465–3471. https://doi.org/10.1152/jn.00190.2010

Martin, P. R., White, A. J. R., Goodchild, A. K., Wilder, H. D., & Sefton, A. E. (1997). Evidence that Blue-on Cells are Part of the Third Geniculocortical Pathway in Primates. *European Journal of Neuroscience*, *9*(7), 1536–1541. https://doi.org/10.1111/j.1460-9568.1997.tb01509.x

Maunsell, J. H. R. (1987). Physiological Evidence for Two Visual Subsystems. In L. M. Vaina (Ed.), *Matters of Intelligence: Conceptual Structures in Cognitive Neuroscience* (pp. 59–87). Springer Netherlands. https://doi.org/10.1007/978-94-009-3833-5_3

McKee, S. P., & Taylor, D. G. (1984). Discrimination of time: Comparison of foveal and peripheral sensitivity. *JOSA A*, *1*(6), 620–627. https://doi.org/10.1364/JOSAA.1.000620

McLoughlin, N., & Schiessl, I. (2006). Orientation selectivity in the common marmoset (Callithrix jacchus): The periodicity of orientation columns in V1 and V2. *NeuroImage*, *31*(1), 76–85. https://doi.org/10.1016/j.neuroimage.2005.12.054

Min, S. H., Gong, L., Baldwin, A. S., Reynaud, A., He, Z., Zhou, J., & Hess, R. F. (2020). *Ocular Dominance Plasticity: Measurement Reliability and Variability* [Preprint]. Neuroscience. https://doi.org/10.1101/2020.07.27.211144

Min, S. H., Gong, L., Baldwin, A. S., Reynaud, A., He, Z., Zhou, J., & Hess, R. F. (2021). Some psychophysical tasks measure ocular dominance plasticity more reliably than others. *Journal of Vision*, *21*(8), 20–20. https://doi.org/10.1167/jov.21.8.20

Mishkin, M., Ungerleider, L. G., & Macko, K. A. (1983). Object vision and spatial vision: Two cortical pathways. *Trends in Neurosciences*, *6*, 414–417. https://doi.org/10.1016/0166-2236(83)90190-X

Moeller, S., Pisharady, P. K., Ramanna, S., Lenglet, C., Wu, X., Dowdle, L., Yacoub, E., Uğurbil, K., & Akçakaya, M. (2021). NOise reduction with DIstribution Corrected (NORDIC) PCA in dMRI with complex-valued parameter-free locally low-rank processing. *NeuroImage*, *226*, 117539. https://doi.org/10.1016/j.neuroimage.2020.117539

Mugler III, J. P., & Brookeman, J. R. (1990). Three-dimensional magnetization-prepared rapid gradient-echo imaging (3D MP RAGE). *Magnetic Resonance in Medicine*,

15(1), 152–157. https://doi.org/10.1002/mrm.1910150117

Mullen, K. T. (1985). The contrast sensitivity of human colour vision to red-green and blue-yellow chromatic gratings. *The Journal of Physiology*, *359*(1), 381–400. https://doi.org/10.1113/jphysiol.1985.sp015591

Mullen, K. T. (1991). Colour vision as a post-receptoral specialization of the central visual field. *Vision Research*, *31*(1), 119–130. https://doi.org/10.1016/0042-6989(91)90079-K

Mullen, K. T., & Kingdom, F. A. A. (1996). Losses in Peripheral Colour Sensitivity Predicted from “Hit and Miss” Post-receptoral Cone Connections. *Vision Research*, *36*(13), 1995–2000. https://doi.org/10.1016/0042-6989(95)00261-8

Mullen, K. T., & Kingdom, F. a. A. (2002). Differential distributions of red–green and blue–yellow cone opponency across the visual field. *Visual Neuroscience*, *19*(1), 109–118. https://doi.org/10.1017/S0952523802191103

Murphy, K. M., Duffy, K. R., Jones, D. G., & Mitchell, D. E. (2001). Development of Cytochrome Oxidase Blobs in Visual Cortex of Normal and Visually Deprived Cats. *Cerebral Cortex*, *11*(2), 122–135. https://doi.org/10.1093/cercor/11.2.122

Nasr, S., Polimeni, J. R., & Tootell, R. B. H. (2016). Interdigitated Color- and Disparity-Selective Columns within Human Visual Cortical Areas V2 and V3. *Journal of Neuroscience*, *36*(6), 1841–1857. https://doi.org/10.1523/JNEUROSCI.3518-15.2016

Nasr, S., & Tootell, R. B. H. (2018). Visual field biases for near and far stimuli in disparity selective columns in human visual cortex. *NeuroImage*, *168*, 358–365. https://doi.org/10.1016/j.neuroimage.2016.09.012

Nassi, J. J., & Callaway, E. M. (2007). Specialized Circuits from Primary Visual Cortex to V2 and Area MT. *Neuron*, *55*(5), 799–808. https://doi.org/10.1016/j.neuron.2007.07.037

Nassi, J. J., & Callaway, E. M. (2009). Parallel processing strategies of the primate visual system. *Nature Reviews Neuroscience*, *10*(5), Article 5. https://doi.org/10.1038/nrn2619

Navarro, K. T., Sanchez, M. J., Engel, S. A., Olman, C. A., & Weldon, K. B. (2021). Depth-dependent functional MRI responses to chromatic and achromatic stimuli throughout V1 and V2. *NeuroImage*, *226*, 117520. https://doi.org/10.1016/j.neuroimage.2020.117520

Newton, J. R., & Eskew, R. T. (2003). Chromatic detection and discrimination in the periphery: A postreceptoral loss of color sensitivity. *Visual Neuroscience*, *20*(5), 511–521. https://doi.org/10.1017/S0952523803205058

Norton, T. T., & Casagrande, V. A. (1982). Laminar organization of receptive-field properties in lateral geniculate nucleus of bush baby (Galago crassicaudatus). *Journal of Neurophysiology*, *47*(4), 715–741. https://doi.org/10.1152/jn.1982.47.4.715

O'Herron, P., Chhatbar, P. Y., Levy, M., Shen, Z., Schramm, A. E., Lu, Z., & Kara, P. (2016). Neural correlates of single-vessel haemodynamic responses in vivo. *Nature*, *534*(7607), Article 7607. https://doi.org/10.1038/nature17965

Ohki, K., Chung, S., Kara, P., Hübener, M., Bonhoeffer, T., & Reid, R. C. (2006). Highly ordered arrangement of single neurons in orientation pinwheels. *Nature*, *442*(7105), Article 7105. https://doi.org/10.1038/nature05019

Okamoto, M., Naito, T., Sadakane, O., Osaki, H., & Sato, H. (2009). Surround suppression sharpens orientation tuning in the cat primary visual cortex. *European Journal of Neuroscience*, *29*(5), 1035–1046. https://doi.org/10.1111/j.1460-9568.2009.06645.x

Olman, C. A., Bao, P., Engel, S. A., Grant, A. N., Purington, C., Qiu, C., Schallmo, M.-P., & Tjan, B. S. (2018). Hemifield columns co-opt ocular dominance column structure in human achiasma. *NeuroImage*, *164*, 59–66. https://doi.org/10.1016/j.neuroimage.2016.12.063

Olman, C. A., Harel, N., Feinberg, D. A., He, S., Zhang, P., Ugurbil, K., & Yacoub, E. (2012). Layer-Specific fMRI Reflects Different Neuronal Computations at Different Depths in Human V1. *PLOS ONE*, *7*(3), e32536. https://doi.org/10.1371/journal.pone.0032536

Olman, C. A., Inati, S., & Heeger, D. J. (2007). The effect of large veins on spatial localization with GE BOLD at 3 T: Displacement, not blurring. *NeuroImage*, *34*(3), 1126–1135. https://doi.org/10.1016/j.neuroimage.2006.08.045

Olman, C. A., Van de Moortele, P.-F., Schumacher, J. F., Guy, J. R., Uğurbil, K., & Yacoub, E. (2010). Retinotopic mapping with spin echo BOLD at 7T. *Magnetic Resonance Imaging*, *28*(9), 1258–1269. https://doi.org/10.1016/j.mri.2010.06.001

Ooi, T. L., & He, Z. J. (2020). Sensory Eye Dominance: Relationship Between Eye and Brain. *Eye and Brain*, *12*, 25–31. https://doi.org/10.2147/EB.S176931

Paffen, C. L. E., Verstraten, F. A. J., & Vidnyánszky, Z. (2008). Attention-based perceptual learning increases binocular rivalry suppression of irrelevant visual features. *Journal of Vision*, *8*(4), 25–25. https://doi.org/10.1167/8.4.25

Peirce, J., Gray, J. R., Simpson, S., MacAskill, M., Höchenberger, R., Sogo, H., Kastman, E., & Lindeløv, J. K. (2019). PsychoPy2: Experiments in behavior made easy. *Behavior Research Methods*, *51*(1), 195–203. https://doi.org/10.3758/s13428-018-01193-y

Qiu, S. X., Caldwell, C. L., You, J. Y., & Mendola, J. D. (2020). Binocular rivalry from luminance and contrast. *Vision Research*, *175*, 41–50. https://doi.org/10.1016/j.visres.2020.06.006

Ringach, D. L., Hawken, M. J., & Shapley, R. (2003). Dynamics of Orientation Tuning in Macaque V1: The Role of Global and Tuned Suppression. *Journal of Neurophysiology*, *90*(1), 342–352. https://doi.org/10.1152/jn.01018.2002

Ringach, D. L., Shapley, R. M., & Hawken, M. J. (2002). Orientation Selectivity in Macaque V1: Diversity and Laminar Dependence. *Journal of Neuroscience*, *22*(13), 5639–5651. https://doi.org/10.1523/JNEUROSCI.22-13-05639.2002

Roe, A. W., & Ts'o, D. Y. (1995). Visual topography in primate V2: Multiple representation across functional stripes. *Journal of Neuroscience*, *15*(5), 3689–3715. https://doi.org/10.1523/JNEUROSCI.15-05-03689.1995

Roth, Z. N., Heeger, D. J., & Merriam, E. P. (2018). Stimulus vignetting and orientation selectivity in human visual cortex. *ELife*, *7*, e37241. https://doi.org/10.7554/eLife.37241

Roth, Z. N., Kay, K., & Merriam, E. P. (2022). Natural scene sampling reveals reliable coarse-scale orientation tuning in human V1. *Nature Communications*, *13*(1), Article 1. https://doi.org/10.1038/s41467-022-34134-7

Salzmann, M. F. V., Bartels, A., Logothetis, N. K., & Schüz, A. (2012). Color Blobs in

Cortical Areas V1 and V2 of the New World Monkey Callithrix jacchus, Revealed by Non-Differential Optical Imaging. *Journal of Neuroscience*, *32*(23), 7881–7894. https://doi.org/10.1523/JNEUROSCI.4832-11.2012

Sasaki, Y., Rajimehr, R., Kim, B. W., Ekstrom, L. B., Vanduffel, W., & Tootell, R. B. H. (2006). The Radial Bias: A Different Slant on Visual Orientation Sensitivity in Human and Nonhuman Primates. *Neuron*, *51*(5), 661–670. https://doi.org/10.1016/j.neuron.2006.07.021

Schiller, P. H., & Logothetis, N. K. (1990). The color-opponent and broad-band channels of the primate visual system. *Trends in Neurosciences*, *13*(10), 392–398. https://doi.org/10.1016/0166-2236(90)90117-S

Schwartz, O., Hsu, A., & Dayan, P. (2007). Space and time in visual context. *Nature Reviews Neuroscience*, *8*(7), Article 7. https://doi.org/10.1038/nrn2155

Serences, J. T., Saproo, S., Scolari, M., Ho, T., & Muftuler, L. T. (2009). Estimating the influence of attention on population codes in human visual cortex using voxel-based tuning functions. *NeuroImage*, *44*(1), 223–231. https://doi.org/10.1016/j.neuroimage.2008.07.043

Shapley, R., Hawken, M., & Ringach, D. L. (2003). Dynamics of Orientation Selectivity in the Primary Visual Cortex and the Importance of Cortical Inhibition. *Neuron*, *38*(5), 689–699. https://doi.org/10.1016/S0896-6273(03)00332-5

Shipp, S., & Zeki, S. (1985). Segregation of pathways leading from area V2 to areas V4 and V5 of macaque monkey visual cortex. *Nature*, *315*(6017), Article 6017. https://doi.org/10.1038/315322a0

Silson, E. H., Chan, A. W.-Y., Reynolds, R. C., Kravitz, D. J., & Baker, C. I. (2015). A

Retinotopic Basis for the Division of High-Level Scene Processing between Lateral and Ventral Human Occipitotemporal Cortex. *Journal of Neuroscience*, *35*(34), 11921–11935. https://doi.org/10.1523/JNEUROSCI.0137-15.2015

Silveira, L. C. L., Saito, C. A., Lee, B. B., Kremers, J., da Silva Filho, M., Kilavik, B. E., Yamada, E. S., & Perry, V. H. (2004). Morphology and physiology of primate M- and P-cells. In *Progress in Brain Research* (Vol. 144, pp. 21–46). Elsevier. https://doi.org/10.1016/S0079-6123(03)14402-0

Sincich, L. C., & Horton, J. C. (2002). Divided by Cytochrome Oxidase: A Map of the Projections from V1 to V2 in Macaques. *Science*, *295*(5560), 1734–1737. https://doi.org/10.1126/science.1067902

Sincich, L. C., Jocson, C. M., & Horton, J. C. (2010). V1 Interpatch Projections to V2 Thick Stripes and Pale Stripes. *Journal of Neuroscience*, *30*(20), 6963–6974. https://doi.org/10.1523/JNEUROSCI.5506-09.2010

Singer, W. (1981). Topographic organization of orientation columns in the cat visual cortex. *Experimental Brain Research*, *44*(4), 431–436. https://doi.org/10.1007/BF00238836

Snowden, R. J., & Hess, R. F. (1992). Temporal frequency filters in the human peripheral visual field. *Vision Research*, *32*(1), 61–72. https://doi.org/10.1016/0042-6989(92)90113-W

Sobel, K. V., & Blake, R. (2002). How Context Influences Predominance during Binocular Rivalry. *Perception*, *31*(7), 813–824. https://doi.org/10.1068/p3279

Sun, P., Gardner, J. L., Costagli, M., Ueno, K., Waggoner, R. A., Tanaka, K., & Cheng, K. (2013). Demonstration of Tuning to Stimulus Orientation in the Human Visual

Cortex: A High-Resolution fMRI Study with a Novel Continuous and Periodic Stimulation Paradigm. *Cerebral Cortex*, *23*(7), 1618–1629. https://doi.org/10.1093/cercor/bhs149

Suzuki, S., & Grabowecky, M. (2007). Long-Term Speeding in Perceptual Switches Mediated by Attention-Dependent Plasticity in Cortical Visual Processing. *Neuron*, *56*(4), 741–753. https://doi.org/10.1016/j.neuron.2007.09.028

Swindale, N. V. (1998). Orientation tuning curves: Empirical description and estimation of parameters. *Biological Cybernetics*, *78*(1), 45–56. https://doi.org/10.1007/s004220050411

Taylor, M. M., & Creelman, C. D. (1967). PEST: Efficient Estimates on Probability Functions. *The Journal of the Acoustical Society of America*, *41*(4A), 782–787. https://doi.org/10.1121/1.1910407

Tong, F., & Engel, S. A. (2001). Interocular rivalry revealed in the human cortical blind-spot representation. *Nature*, *411*(6834), Article 6834. https://doi.org/10.1038/35075583

Tong, F., Meng, M., & Blake, R. (2006). Neural bases of binocular rivalry. *Trends in Cognitive Sciences*, *10*(11), 502–511. https://doi.org/10.1016/j.tics.2006.09.003

Tootell, R. B. H., & Nasr, S. (2017). Columnar Segregation of Magnocellular and Parvocellular Streams in Human Extrastriate Cortex. *Journal of Neuroscience*, *37*(33), 8014–8032. https://doi.org/10.1523/JNEUROSCI.0690-17.2017

Tootell, R. B. H., Silverman, M. S., De Valois, R. L., & Jacobs, G. H. (1983). Functional Organization of the Second Cortical Visual Area in Primates. *Science*, *220*(4598), 737–739. https://doi.org/10.1126/science.6301017

Tootell, R. B. H., & Taylor, J. B. (1995). Anatomical Evidence for MT and Additional Cortical Visual Areas in Humans. *Cerebral Cortex*, *5*(1), 39–55. https://doi.org/10.1093/cercor/5.1.39

Uğurbil, K., Adriany, G., Andersen, P., Chen, W., Garwood, M., Gruetter, R., Henry, P.-G., Kim, S.-G., Lieu, H., Tkac, I., Vaughan, T., Van De Moortele, P.-F., Yacoub, E., & Zhu, X.-H. (2003). Ultrahigh field magnetic resonance imaging and spectroscopy. *Magnetic Resonance Imaging*, *21*(10), 1263–1281. https://doi.org/10.1016/j.mri.2003.08.027

Uludağ, K., & Blinder, P. (2018). Linking brain vascular physiology to hemodynamic response in ultra-high field MRI. *NeuroImage*, *168*, 279–295. https://doi.org/10.1016/j.neuroimage.2017.02.063

van der Zwaag, W., Buur, P. F., Fracasso, A., van Doesum, T., Uludağ, K., Versluis, M. J., & Marques, J. P. (2018). Distortion-matched T1 maps and unbiased T1-weighted images as anatomical reference for high-resolution fMRI. *NeuroImage*, *176*, 41–55. https://doi.org/10.1016/j.neuroimage.2018.04.026

Van Hooser, S. D., Roy, A., Rhodes, H. J., Culp, J. H., & Fitzpatrick, D. (2013). Transformation of receptive field properties from lateral geniculate nucleus to superficial V1 in the tree shrew. *Journal of Neuroscience*, *33*(28), 11494–11505. Scopus. https://doi.org/10.1523/JNEUROSCI.1464-13.2013

Vanduffel, W., Tootell, R. B. H., Schoups, A. A., & Orban, G. A. (2002). The Organization of Orientation Selectivity Throughout Macaque Visual Cortex. *Cerebral Cortex*, *12*(6), 647–662. https://doi.org/10.1093/cercor/12.6.647

Vanni, S., Henriksson, L., Viikari, M., & James, A. C. (2006). Retinotopic distribution of

chromatic responses in human primary visual cortex. *European Journal of Neuroscience*, *24*(6), 1821–1831. https://doi.org/10.1111/j.1460-9568.2006.05070.x

Vizioli, L., Moeller, S., Dowdle, L., Akçakaya, M., De Martino, F., Yacoub, E., & Uğurbil, K. (2021). Lowering the thermal noise barrier in functional brain mapping with magnetic resonance imaging. *Nature Communications*, *12*(1), Article 1. https://doi.org/10.1038/s41467-021-25431-8

Waehnert, M. D., Dinse, J., Weiss, M., Streicher, M. N., Waehnert, P., Geyer, S., Turner, R., & Bazin, P.-L. (2014). Anatomically motivated modeling of cortical laminae. *NeuroImage*, *93*, 210–220. https://doi.org/10.1016/j.neuroimage.2013.03.078

Wang, M., McGraw, P., & Ledgeway, T. (2021). Attentional eye selection modulates sensory eye dominance. *Vision Research*, *188*, 10–25. https://doi.org/10.1016/j.visres.2021.06.006

Weldon, K. B., Burton, P. C., Grant, A. N., Yacoub, E., & Olman, C. A. (2019). *Defining region-specific masks for reliable depth-dependent analysis of fMRI data* (p. 557363). bioRxiv. https://doi.org/10.1101/557363

Weng, X., Lin, Q., Ma, Y., Peng, Y., Hu, Y., Zhou, K., Shen, F., Wang, H., & Wang, Z. (2019). Effects of Hunger on Visual Perception in Binocular Rivalry. *Frontiers in Psychology*, *10*, 418. https://doi.org/10.3389/fpsyg.2019.00418

Xiao, Y., & Felleman, D. J. (2004). Projections from primary visual cortex to cytochrome oxidase thin stripes and interstripes of macaque visual area 2. *Proceedings of the National Academy of Sciences*, *101*(18), 7147–7151.

https://doi.org/10.1073/pnas.0402052101

Xu, J. P., He, Z. J., & Ooi, T. L. (2010). Effectively Reducing Sensory Eye Dominance with a Push-Pull Perceptual Learning Protocol. *Current Biology*, *20*(20), 1864–1868. https://doi.org/10.1016/j.cub.2010.09.043

Yabuta, N. H., & Callaway, E. M. (1998). Functional Streams and Local Connections of Layer 4C Neurons in Primary Visual Cortex of the Macaque Monkey. *Journal of Neuroscience*, *18*(22), 9489–9499. https://doi.org/10.1523/JNEUROSCI.18-22-09489.1998

Yabuta, N. H., Sawatari, A., & Callaway, E. M. (2001). Two Functional Channels from Primary Visual Cortex to Dorsal Visual Cortical Areas. *Science*, *292*(5515), 297–300. https://doi.org/10.1126/science.1057916

Yacoub, E., Harel, N., & Uğurbil, K. (2008). High-field fMRI unveils orientation columns in humans. *Proceedings of the National Academy of Sciences*, *105*(30), 10607–10612. https://doi.org/10.1073/pnas.0804110105